Quantifying uncertainty in the process-structure relationship for Al-Cu solidification

Anh Tran[1], Dehao Liu[1], Hoang Tran[2], and Yan Wang[*1]

[1] *George Woodruff School of Mechanical Engineering*
Georgia Institute of Technology, Atlanta, GA
[2] *Department of Computational and Applied Mathematics*
Oak Ridge National Labs, Oak Ridge, TN

May 7, 2019

Abstract

Phase field method (PFM) is a simulation tool to predict the microstructural evolution during solidification and helpful to establish the process-structure relationship for alloys. The robustness of the relationship however is affected by model-form and parameter uncertainties in PFM. In this paper, the uncertainty associated with the thermodynamic and process parameters of PFM is studied and quantified. Surrogate modeling is used to interpolate four quantities of interests (QoIs), including dendritic perimeter, area, primary arm length, and solute segregation, as functions of thermodynamic and process parameters. A sparse grid approach is applied to mitigate the curse-of-dimensionality computational burden in uncertainty quantification. Polynomial chaos expansion is employed to obtain the probability density functions of the QoIs. The effect of parameter uncertainty on the Al-Cu dendritic growth during solidification simulation are investigated. The results show that the dendritic morphology varies significantly with respect to the interface mobility and the initial temperature.

[*]Corresponding author: yan.wang@me.gatech.edu

1 Introduction

Phase field method (PFM) is a widely used simulation tool for studying the evolution of microstructures during solidification. The microstructure evolution, or more specifically the dendritic growth along time, is modeled, and the characteristics of microstructures can be predicted. Thus the process-structure relationship for solidification can be established via simulation. Uncertainty quantification (UQ) however plays a critical role in using the predicted structure-property relationship for process design, given the model-form and parameter uncertainties in PFM. Model-form uncertainty is due to simplification, approximation, and subjectivity during the modeling process, whereas parameter uncertainty is the result of model calibration.

There are various sources of model-form uncertainty in PFM. Simplifications are the major ones. First, solidification is a complex physical process which requires a multi-physics approach to model the dynamics of thermal distributions, velocity and pressure of fluid flows, latent heat of phase transition, and thermoelectric current, which all affect the nucleation and growth of grains [1]. PFM itself however only provides a simplified view of the physics with various assumptions. Uncertainty thus arises from the separation of physics. Second, in a complete solidification model, multi-scale phenomena need to be considered, including atomic clustering and crystallization in nucleation, as well as liquid-solid interface mobility at the atomistic scale. Existing PFM models focus on mesoscale and use thermodynamics nucleation models in combination with empirical methods. Similarly, the interface mobility is usually simplified to be constant and temperature-independent with empirical values. The dentritic growth and morphology in solidification can be fairly unstable and caused by many factors such as impurities as nucleation seeds, locally trapped supercooled liquid, surface tension, interfacial anisotropy, interface mobility, and others. The separation of scales introduces model-form uncertainty. Model-form uncertainty also comes from approximations. First, truncations are always applied in the formulation of partial differential equations for complex physics during mathematical modeling, which keep equations at low integer orders. Truncations are also applied in functional and reciprocal spaces during the computational modeling process. Second, numerical treatment in solving the equations introduces additional approximation and discretization errors which lead to numerical instability, such as von Neumann instability in the explicit time-integration scheme. Particularly for PFM, the diffuse interface thickness in the simulation model is typically two orders of magnitude higher than the physical interface thickness, which also introduces

numerical errors, although anti-trapping current is usually introduced to eliminate the numerical solute trapping. In addition, model-form uncertainty in PFM can be the bias introduced with subjective choices of free energy functions with different forms of multi-well and multi-obstacle for different phases.

Parameter uncertainty of PFM is introduced during the model calibration process. First, PFM often relies on computational thermodynamics methods (e.g., CALPHAD), molecular dynamics, and first-principles calculations for phase equilibrium thermodynamic parameters. The model-form and parameter uncertainties from these models propagate and become the parameter uncertainty of the PFM model. Second, for empirical methods where model parameters are adjusted so that predictions match experimental observations, uncertainty originated from the systematic and random errors in experimental measurements propagates to the PFM model as the parameter uncertainty.

Given the various sources of uncertainty in PFM, the accuracy and robustness of predictions on dendritic growth and microstructures are the major challenges in the investigation of process-structure-property linkages based on simulations. When the linkages are applied to process design and optimization, uncertainties need to be taken into account for robustness. In this study, we focus on the parameter uncertainty in PFM, particularly the effects of process parameters and thermodynamic parameters associated with materials. Surrogate based UQ methods including sparse grid and polynomial chaos expansion are applied here. Note that model-form uncertainty is mainly epistemic, whereas parameter uncertainty is a combination of epistemic and aleatory ones. The study of model-form uncertainty can be based on probabilistic and non-probabilistic UQ methods.

UQ for materials modeling has attracted research attentions in recent years [2, 3, 4]. Particularly at atomistic scale, the major sources of model-form and parameter uncertainty in first-principles density functional theory (DFT) include the exchange-correlation functionals, pseudopotentials and nonzero temperature approximations, as well as calibration errors [5, 6]. UQ methods such as Bayesian error estimation [7], sensitivity analysis [8], and Gaussian process [9, 10] have been applied to quantify the uncertainty associated with energy calculation in DFT. The major sources of uncertainty in molecular dynamics are inaccurate inter-atomic potentials and the bias introduced in simulated small sizes and short time scales. UQ methods such as polynomial chaos expansion [11, 12], statistical regression [13], Bayesian calibration [14, 15, 16, 17, 18], interval bound analysis [19, 20], and local sensitivity analysis and perturbation [21, 22] have been applied to quantify simulation errors.

The uncertainty in kinetic Monte Carlo simulation is mainly due to event independence assumption, incomplete knowledge of event catalog, and imprecise kinetic rates. Random set sampling approach [23] was applied to quantify the prediction errors. In addition, some UQ issues which are unique in materials modeling, such as cross-scale model validation [24] and cross-scale calibration [25] with model-form discrepancy, still require further studies. Note that the model-form and parameter uncertainties of the above atomistic models can propagate to mesoscale PFM models as parameter uncertainty when the atomistic models are used to estimate and calibrate the PFM parameters.

In PFM simulation, the instability of morphology prediction is caused by both model-form and parameter uncertainties. To mitigate the effect of model-form uncertainty due to missing physics and information, stochastic [26, 27] and fractional order differential equations [28, 29] can be introduced. Empirical model adjustment such as anti-trapping current term [30] can be added. In this paper, we focus on the effect of parameter uncertainty. The uncertainty effects of process and thermodynamic parameters on the microstructures of Al-4wt%Cu binary alloy during solidification simulation are studied. The microstructures are quantified by four quantities of interest (QoIs) including dendritic area, dendritic perimeter, the segregation of Cu at solid-liquid interface, and the length of primary arm of dendrite. An image processing pipeline is utilized to automatically quantify the variations of the four aforementioned QoIs. The sparse grid (SG) method is used to interpolate these QoIs in high-dimensional input space and to reduce the computational burden of performing a large number of PFM simulations. The representative dendritic morphology corresponding to the SG nodes clearly demonstrates the impact of the input parameters on the dendritic growth. The dendritic morphology varies significantly with respect to the interface mobility M_ϕ, which is a thermodynamic parameter, and the initial temperature T_0, which is a process parameter. The polynomial chaos expansion (PCE) framework is employed to quantify the uncertainty associated with the QoIs, where the process parameters are assumed to be deterministic and controllable, whereas the thermodynamic parameters are assumed to be random. The UQ study provides insights of the robustness in the process-structure relationship for Al-4wt%Cu binary alloys.

In the remainder of the paper, Section 3 introduces the formulation of SG for high-dimensional interpolation, and briefly discusses the formulation of PCE framework in a UQ problem. Section 4 describes the details about the PFM to study the dendritic evolution, as well as the automatic post-processing pipeline, in which four physical QoIs are extracted and studied as functions of process

and thermodynamic parameters. Section 5 analyzes the UQ results for two separate cases. In the first case (Section 5.1), the QoIs are represented as high-dimensional interpolation quantities and the one-at-a-time variations of the QoIs with respect to input parameters are investigated. In the second case (Section 5.2), the thermodynamic parameters are treated as random inputs, and the probability density functions (PDFs) of the QoIs at different values of process parameters are generated. In Section 6, the results are discussed. Section 7 concludes the paper.

2 Background

2.1 Instability nature of dendritic growth and numerical stability of phase field formulation

Model-form and parameter uncertainties in PFM can lead to perturbation and inaccuracy of dendritic morphology predictions. Dendritic growth is by nature an unstable phenomenon. During the cooling process, it is possible for a material to remain in its (thermodynamically metastable) liquid state even below the melting temperature. The solidification process can occur homogeneously after sufficient cooling, or heterogeneously by a nucleated seed within the supercooled liquid [31]. The later one induces an unstable dendritic growth. The solidification can be divided into either a stable or unstable process. In a stable solidification process or Stefan problem, the kinetic mobility and surface tension are ignored, resulting in a reduced perturbation on the interface. When the heat is conducted away from the solid-liquid interface and the surface tension and kinetic mobility cannot be neglected, the solidification becomes unstable. When the undercooling is large enough, the dendritic growth becomes dominant. During unstable dendritic growth, any statistic fluctuations can be amplified, which reflects in the formation of secondary arms. Jaafar et al. [31] provides a comprehensive review on dendritic growth instability, including Mullins-Sekerka [32] and interfacial instabilities, as well as the history and evolution of Gibbs-Thomson condition. The interfacial anisotropy, due to the presence of the crystal lattice in solid phase, also plays an important role in the dendritic side-branching. Glicksman [33] noted the promotion of dendritic side-branching is rooted from applying the anisotropic of Gibbs-Thomson condition to an interface with both strong shape anisotropy and crystal's energy anisotropy, resulting in a pulsatile tip motion.

To simulate solidification, methods of front tracking, enthalpy, lever set, cellular automaton,

and phase field have been developed. PFM is the most used one and regarded as the most accurate method, even though it is computationally more expensive than the other. Nevertheless, model errors in PFM can cause instability of simulated dendritic growth, exhibited as the interfacial, capillary, and chemical instabilities. Model-form errors are from the derivation of the partial differential equations, and numerical treatment in solving them. Some research efforts have been done to improve the numerical stability. Karma [34] proposed a PFM formulation that uses a thin-interface and added an anti-trapping current term to model the temperature jump across the interface and correct the heat conservation and the surface diffusion at the interface for binary dilute alloys. Kim [35] extended the method of Karma [34] by generalizing the anti-trapping term for arbitrary multicomponent alloys. Tianden et al. [36] and Eiken et al. [37] proposed a thermodynamically consistent PFM for multiphase and multicomponent systems.

2.2 Sensitivity study of uncertainty on phase-field simulation of dendritic growth

To model the interface stability because of model-form uncertainty, some approaches to enhance the PFM models have been proposed. One of the perturbation theories of interface stability is called Mullins-Sekerka instability [38, 39, 32], which determines if a small-amplitude perturbation will be enhanced in time and destabilize the interface, or decay and leave the initial interface unchanged and morphologically stable. The time dependent marginal stability theory developed by Langer and Muller-Krumbhaar [40, 41, 42] can be used as a criterion for selection of the operating state of the dendrite tip, which is related to the dendrite tip radius and velocity.

Sensitivity analysis (SA) has been applied in PFM to understand the effect of input parameters on simulation results. Xing et al. [43] investigated the columnar dendritic growth competition with respect to the orientation in Al-4wt%Cu alloy. Takaki et al. [44] proposed a coupled phase field-lattice Boltzmann model to study the effect of solute expansion factor on dendritic morphology, tip velocity, and concentration of the Al-4wt%Cu for dendritic growth with natural convection. Qi et al. [45] studied the effects of different natural convection schemes and solid motion on the dendritic tip growth velocity of the Al-4wt%Cu alloy using PFM and computational fluid dynamics and concluded that when the dendrite is mobile, the tip growth velocity is sensitive to the natural convection schemes. Liu and Wang [46, 1] proposed a framework called phase field and thermal lattice Boltzmann method to investigate the effects of cooling rate and latent heat on the dendritic

morphology, concentration, and temperature fields of Al-4wt%Cu alloy. Boukellal et al. [47] conducted a SA of the solute composition and the average distance between two nuclei on the dendritic growth of Al-Cu binary alloy using PFM, and proposed a scaling laws for the tip velocity. Fezi and Krane [48] developed a simple 1D solidification model and conducted a uncertainty analysis using Smolyak sparse grid on the positions of the liquidus, the solidus, and the solidification time of alloy 625, with 7 input parameters. Fezi and Krane [49] conducted a sensitivity analysis on the solidification of Al-4.5wt%Cu alloy, with respect to different secondary dendritic arm spacing, equiaxed particle size, and solids fraction in mushy zone, where the QoIs are the macrosegregation number, the Weibull deviation of positive segregation, and the volume fraction of the ingot. Fezi and Krane [50, 51] investigated the effects of microstructural model parameters, thermal boundary conditions, and material properties on the macrosegregation levels and solidification time, and concluded that the macrosegregation are sensitive to the dendrite arm spacing in the mushy zone. Plotkowski and Krane [52] analyzed three two-dimensional Al-4.5wt%Cu solidification models with 7 and 9 input parameters that account for both model-form and parameter uncertainties. However, in existing work, the combined effects of uncertainties associated with thermodynamic and process parameters upon the dendritic morphology using PFM has not been studied. More importantly, the uncertainty in the process-structure relationship for dendritic growth has not been quantified systematically.

3 Stochastic collocation for uncertainty quantification

In this section, we briefly summarize the stochastic collocation technique, which is employed to solve the UQ problem. In this approach, the SG and PCE methods are combined to efficiently quantify the uncertainty of the QoIs.

3.1 Sparse grid method for high-dimensional interpolation

To mitigate the curse of dimensionality, the SG technique is employed to interpolate the QoIs in the high-dimensional domain. We follow the formulation in [53, 54], and use global Lagrange polynomials as basis functions. To be accurate, the interpolating function often needs to be smooth, which is a reasonable assumption for the simulation considered herein. The accuracy of SG method has been studied extensively by Bungartz et al. [55] and Nobile et al [56].

Let f be the function, i.e. QoI, to be interpolate. Assume f is defined on the domain $D = [-1, 1]^d$. Given ensembles $\{f(x_j)\}_{j=1}^m$, the interpolation approach finds an approximation $\mathcal{U}(f)$ of f that fulfills the condition $\mathcal{U}(f)(x_j) = f(x_j)$, $\forall j = 1, \ldots, m$. More specifically, we seek

$$\mathcal{U}(f)(x) = \sum_{j=1}^{m} f(x_j) L_j(x), \tag{1}$$

where $L_j(x)$ are the Lagrange polynomials

$$L_j(x_i) = 1 \quad \text{if} \quad i = j, \quad L_j(x_i) = 0 \quad \text{if} \quad i \neq j, \quad 1 \leq i, j \leq m,$$

whose explicit formulae are known. Interpolation in one dimension ($d = 1$) is well-studied. To extend the method to multiple dimensions ($d > 1$), we need to employ certain tensor product rule. The full tensor product formula is perhaps the most straightforward, as

$$\mathcal{U}^{m_1} \otimes \cdots \otimes \mathcal{U}^{m_d}(f) = \sum_{j_1=1}^{m_1} \cdots \sum_{j_d=1}^{m_d} f(x_{j_1}, \ldots, x_{j_d}) \cdot (L_{j_1} \otimes \cdots \otimes L_{j_d}). \tag{2}$$

Here, $\mathcal{U}^{m_i}(f)$ is one-dimensional Lagrange interpolation in the i-th dimension with $m = m_i$, so the rule just employs univariate interpolations and then fills up D dimension by dimension. Albeit simple, a major drawback of full tensor product is that the total number of points grows very fast in high dimensions.

An alternative and more efficient approach is Smolyak sparse grids interpolation, based on the work by Smolyak in [57]. Instead of taking the full tensor product in Eq. (2), the Smolyak interpolation takes a subset of the full tensor construction described as

$$\mathcal{A}(q, d) = \sum_{q-d+1 \leq |\boldsymbol{i}| \leq q} (-1)^{q-|\boldsymbol{i}|} \cdot \binom{d-1}{q-|\boldsymbol{i}|} \cdot \mathcal{U}^{i_1} \otimes \cdots \otimes \mathcal{U}^{i_d}. \tag{3}$$

see [58], where $q \geq d$ is an integer denoting the level of the construction. To compute the operator $\mathcal{A}(q, d)$, one needs to evaluate f on the set of points

$$\mathcal{H}(q, d) = \bigcup_{q-d+1 \leq |\boldsymbol{i}| \leq q} \left(\mathcal{X}^{i_1} \times \cdots \times \mathcal{X}^{i_d} \right), \tag{4}$$

where $\mathcal{X}^i = \{x_1^i, \ldots, x_{m_i}^i\} \subset [-1, 1]$ is the collection of nodes used by the univariate interpolating operator $\mathcal{U}^i$. This set is a much smaller subset of those required by the full tensor product rule.

In this paper, we opt to use Clenshaw-Curtis points [59], which are the roots of Chebyshev polynomials and specified as

$$x_j^i = -\cos\frac{\pi(j-1)}{m_i - 1}, j = 1, \ldots, m_i, \tag{5}$$

where $x_1^i = 0$ if $m_i = 1$, and $m_i = 2^{i-1} + 1$ for $i > 1$. This rule is very popular in high-dimensional interpolation, due to its stability as well as nested property, i.e., the lower-level grids are subsets of the higher-level grids. Figure 1a and Figure 1b show two examples of 2D and 3D SG, respectively, where the Clenshaw-Curtis nodes are used to construct the SG. To see the reduction in function ensembles by using SG, we compare the number of nodes required by SG and full tensor grid in Table 1. It is possible to construct the interpolation of QoIs with other choices of quadrature rules (e.g., Gauss rules, greedy rules) as well as basis functions (e.g., piecewise polynomials, wavelets). We do not attempt to optimize such choices in this paper and will investigate this in future study.

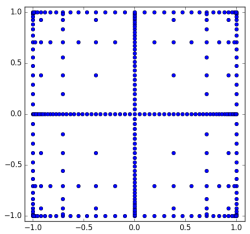

(a) $q = 6$, Clenshaw-Curtis nodes; $d = 2$; number of nodes per main dimension: 65; total number of nodes: 321

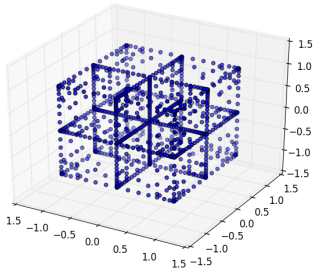

(b) $q = 6$, Clenshaw-Curtis nodes; $d = 3$; number of nodes per main dimension: 321; total number of nodes: 1073;

Figure 1: Example of SG in 2D (a) and 3D (b) for high dimensional interpolation.

3.2 Non-intrusive spectral projection for uncertainty propagation

We rely on spectral representation of uncertainty using the PCE framework and the non-intrusive spectral projection method to compute the PDFs of QoIs. PCE [60, 61] is one of the most widely used UQ methods to propagate uncertainty in physical models and computational simulations. Let θ be the random event in a sample space Ω with probability measure P, and $f(\theta)$ be a second order stochastic process. PCE is a means of representing f parametrically through a set of random

Table 1: The number of nodes used by SG and full tensor grid.

Level	$d=3$		$d=5$		$d=7$	
	SG	full grid	SG	full grid	SG	full grid
0	1	1	1	1	1	1
1	7	27	11	243	15	2,187
2	25	125	61	3,125	113	78,125
3	69	729	241	59,049	589	4,782,969
4	177	4,913	801	1,419,857	2,465	410,338,673
5	441	35,937	2,433	39,135,393	9,017	4.26e+10
6	1,073	274,625	6,993	1,160,290,625	30,241	4.90e+12
7	2,561	2,146,689	19,313	3.57e+10	95,441	5.94e+14
8	6,017	16,974,593	51,713	1.12e+12	287,745	7.40e+16

variables $\{\zeta_i(\theta)\}_{i=1}^d$, $d \in \mathbb{N}$:

$$f(\theta) = \sum_{j=0}^{\infty} \widehat{f}_j \mathbf{\Phi}_j(\boldsymbol{\zeta}(\theta)), \tag{6}$$

where $\mathbf{\Phi}_j(\boldsymbol{\zeta}(\theta))$ are orthogonal polynomials in terms of $\boldsymbol{\zeta} := \{\zeta_i(\theta)\}_{i=1}^d$, i.e.,

$$\langle \mathbf{\Phi}_i \mathbf{\Phi}_j \rangle \neq 0 \quad \text{if} \quad i = j, \quad \langle \mathbf{\Phi}_i \mathbf{\Phi}_j \rangle = 0 \quad \text{if} \quad i \neq j,$$

Here, $\widehat{f}_j$ are the coefficients to be computed, and $\langle \mathbf{\Phi}_i \mathbf{\Phi}_j \rangle := \int_{\theta \in \Omega} \mathbf{\Phi}_i(\boldsymbol{\zeta}) \mathbf{\Phi}_j(\boldsymbol{\zeta}) dP(\theta)$. In practice, the number of terms in (6) are truncated after a finite term P, where $P + 1 = \dfrac{(p+d)!}{p!d!}$, p is the order of PCE, and d is the dimensionality of the problem, resulting in an approximation for finite PCE, as

$$f(\theta) \approx \sum_{j=0}^{P} \widehat{f}_j \mathbf{\Phi}_j(\boldsymbol{\zeta}). \tag{7}$$

The PCE coefficients $\widehat{f}_j$ is determined by projection of (7) onto the polynomial basis $\{\mathbf{\Phi}_j\}$ as

$$\widehat{f}_j = \frac{\langle f \mathbf{\Phi}_j \rangle}{\langle \mathbf{\Phi}_j^2 \rangle}. \tag{8}$$

To compute the PCE coefficients, we apply a non-intrusive spectral projection approach [62, 63, 64] to evaluate the deterministic high-dimensional integrals in the numerators and denominators

of (8). In short, we compute the value of basis functions at the Clenshaw-Curtis nodes to obtain the PDFs using Legendre-Uniform quadratures and interpolate the QoIs through the interpolation process.

4 Phase-field model for dendritic growth simulation

In this paper, we adopted the PFM developed from Steinbach et al. [65, 36, 37], which have been validated against experimental observations [65], where the antitrapping current term is added to ensure equal chemical potential between liquid and solid phases.

The essential component of PFM is a free energy functional that describes the kinetics of phase transition. The free energy functional

$$F = \int_{\Omega} (f^{\mathrm{GB}} + f^{\mathrm{CH}}) dV \tag{9}$$

is defined with an interfacial free energy density f^{GB} and a chemical free energy density f^{CH} in a domain Ω.

A continuous variable named phased field ϕ ($0 \leq \phi \leq 1$) indicates the fraction of solid phase in the simulation domain during the solidification process, and the fraction of liquid phase is $\phi_l = 1 - \phi$. The interfacial free energy density is defined as

$$f^{\mathrm{GB}} = \frac{4\sigma^*(\boldsymbol{n})}{\eta} \left\{ |\nabla\phi|^2 + \frac{\pi^2}{\eta^2}\phi(1-\phi) \right\}, \tag{10}$$

where $\sigma^*(\boldsymbol{n})$ is the anisotropic interfacial energy stiffness, η is the interfacial width, $\boldsymbol{n} = \dfrac{\nabla\phi}{|\nabla\phi|}$ is the local normal direction of the interface. The anisotropic interfacial energy stiffness is defined as

$$\sigma^* = \sigma + \frac{\partial^2 \sigma}{\partial \theta^2} = \sigma_0^*[1 - 3\varepsilon^* + 4\varepsilon^*(n_x^4 + n_y^4)], \tag{11}$$

where σ is the interfacial energy, $\theta = \operatorname{atan}\left(\dfrac{n_y}{n_x}\right)$ indicates the orientation, σ_0^* is the prefactor of interfacial energy stiffness, and ε^* is the anisotropy strength of interfacial energy stiffness, which models the difference between the primary and secondary growth directions of dendrites.

The chemical free energy is the combination of bulk free energies of individual phases as

$$f^{\mathrm{CH}} = h(\phi) f_s(C_s) + h(1-\phi) f_l C_l + \mu[C - (\phi_s C_s + \phi_l C_l)], \tag{12}$$

where C_s and C_l are the compositions of solutions as weight percent (wt%) in solid and liquid phases respectively, which is the amount of solute dissolved in a specific amount of solution. C is the overall composition of a solution in the simulation domain. $f_s(C_s)$ and $f_l(C_l)$ are the chemical bulk free energy densities of solid and liquid phases respectively. μ is the generalized chemical potential of solute introduced as a Lagrange multiplier to conserve the solute mass balance $C = \phi_s C_s + \phi_l C_l$. The weight function

$$h(\phi) = \frac{1}{4}\left[(2\phi - 1)\sqrt{\phi(1-\phi)} + \frac{1}{2}\mathrm{asin}(2\phi - 1)\right] \tag{13}$$

provides the coefficients associated with solid and liquid bulk energies.

The evolution of the phase field is described by

$$\dot{\phi} = M_\phi \left\{\sigma^*(\boldsymbol{n})\left[\nabla^2\phi + \frac{\pi^2}{\eta^2}(\phi - \frac{1}{2})\right] + \frac{\pi}{\eta}\sqrt{\phi(1-\phi)}\Delta G\right\}, \tag{14}$$

where M_ϕ is the coefficient of interface mobility, and the driving force is given by

$$\Delta G = \Delta S(T_m - T + m_l C_l), \tag{15}$$

where $\Delta S = -1 \cdot 10^6 J \cdot K^{-1}$ is the entropy difference between the solid and liquid phase, T_m is the melting temperature of a pure substance, T is the temperature field, and m_l is slope of liquidus. For simplification, the interface mobility is assumed to be constant in this work.

The evolution of composition variable is modeled by

$$\dot{C} = \nabla \cdot [D_l(1-\phi)\nabla C_l] + \nabla \cdot \boldsymbol{j}_{\mathrm{at}}, \tag{16}$$

where $k = \dfrac{C_s}{C_l}$ is the local partition coefficient and D_l is the diffusion coefficient of liquid. Furthermore, $\boldsymbol{j}_{\mathrm{at}}$ is the anti-trapping current and defined as

$$\boldsymbol{j}_{\mathrm{at}} = \frac{\eta}{\pi}\sqrt{\phi(1-\phi)}(C_l - C_s)\dot{\phi}\frac{\nabla\phi}{|\nabla\phi|} \tag{17}$$

which is to eliminate the unphysical solute trapping during the interface diffusion process by removing the anomalous chemical potential jump [35, 66] so that simulations can be done more efficiently with the simulated interface width larger than the physical one. The PFM are solved mainly based on Equation 14 and Equation 16.

The open-source PFM toolkit OpenPhase [67] is used to simulate the two dimensional (2D) dendritic growth of binary alloy Al-4wt%Cu. Table 1 shows the physical properties of Al-4wt%Cu

alloy. In all simulation runs, the grid spacing is $\Delta x = 0.5\mu$m, the time step is $\Delta t = 2 \cdot 10^{-5}$s, and the simulation period is 0.12 s. The length and width of the simulated domain are $L_x = 150\mu$m and $L_y = 150\mu$m in x- ($< 1, 0, 0 >$) and y-directions ($< 0, 1, 0 >$), respectively. In general, the interface width should be at least $3\Delta x$ to guarantee the convergence of simulation. Therefore, the interface width is $\eta = 5\Delta x = 2.5\mu$m. The initial diameter D should be larger than the interface width and $D = 5\mu$m is determined in this work. The initial position of the seed is at the center of the simulation box. The initial concentration of Cu is $C_0 = 4$wt% for the liquid melt. For phase field ϕ and concentration C, zero Neumann conditions are set at all boundaries.

Table 2 lists the physical parameters of the Al-4wt%Cu alloy concerned in the study. The dendritic growth of Al-4wt%Cu is investigated through a parametric study of PFM, where the input parameters are varied, and the QoIs are investigated using an automatic post-processing pipeline. Table 3 lists the ranges of input parameters and their physical meanings in the PFM study.

The ranges of input parameters are determined based on the values used in other simulation and experimental studies [68] of solidification. Because the number of samples is limited in the literature, the parameters used in this work are assumed to be uniformly distributed based on the principle of maximum entropy.

Table 2: The physical properties of Al-4wt%Cu alloy.

Symbol	Physical meaning	Value	Unit
T_m	Melting point of pure Al	933.6	K
ρ	Density of liquid	2700	kg/m^3
m_l	Slope of liquidus	-2.6	K/wt%
k	Partition coefficient	0.14	
D_l	Diffusivity of liquid	$3.0 \cdot 10^{-9}$	m^2/s
σ_0^*	Prefactor of interfacial energy stiffness	0.24	J/m^2
ε^*	Interfacial energy stiffness anisotropy	0.35	
M_ϕ	Interface mobility	$4 \cdot 10^{-9}$	m^4/(J$\cdot$ s)

Table 3: Input parameters and their respective ranges.

Symbol	Physical meaning	Lower bound	Upper bound	Unit
$\frac{\partial T}{\partial t}$	Cooling rate	-20	-10	K/s
T_0	Initial temperature	915	920	K
σ_0^*	Prefactor of interfacial energy stiffness	0.22	0.26	J/m^2
ε^*	Interface anisotropy	0.30	0.40	
M_ϕ	Interface mobility	$3 \cdot 10^{-9}$	$5 \cdot 10^{-9}$	m^4/(J$\cdot$ s)

4.1 Simulation procedure

Figure 2a and Figure 2b show an example of dendritic growth at different snapshots in the 2D PFM simulations. The primary and secondary dendritic arms are observed. The input parameters listed in Table 3 have direct impact on the geometry and shape of the dendritic growth. An automatic post-processing pipeline is devised to extract the QoIs that describe the dendrite.

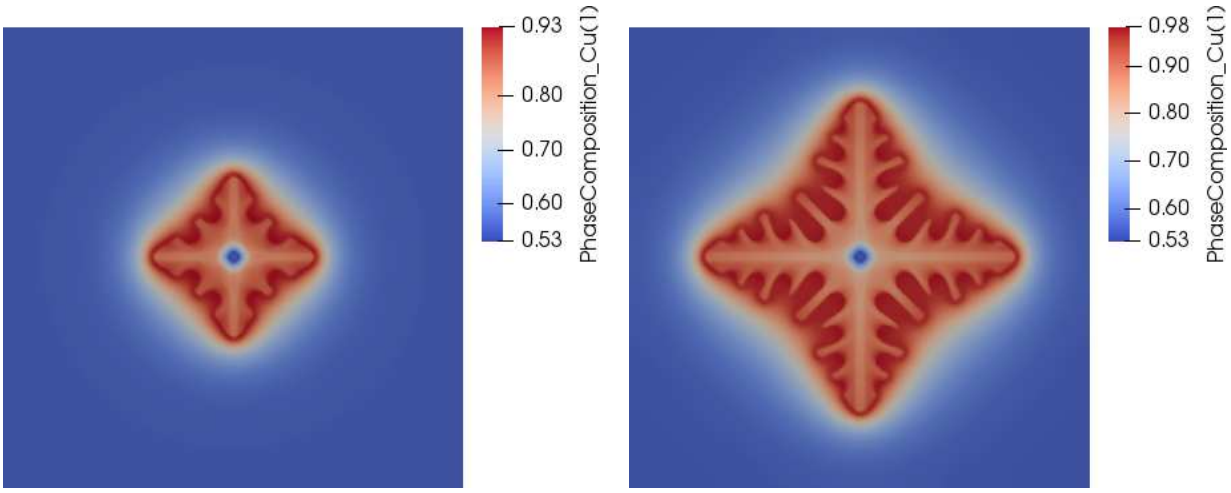

(a) An example of dendritic growth at timestep 3000.

(b) An example of dendritic growth at timestep 6000.

Figure 2: Dendritic growth of binary alloy Al-4wt%Cu at different snapshots.

A level-seven SG for five-dimensional space is constructed based on Clenshaw-Curtis rule [59], where the nested Chebyshev nodes are chosen. Tasmanian package [69, 70, 71, 72] is used to construct and evaluate for high-dimensional interpolation. The construction of SG results in 19,313 nodes,

which correspond to different sets of inputs for the PFM. As shown in Table 1, the use of level-seven full tensor grid would require 3.57×10^{10} nodes for comparable results. At each node, a PFM simulation is performed, and the QoIs are collected once the simulation is finished. The process is automated using Bash/Shell and Python scripts. The mappings from the process parameter space to the microstructural descriptor space are known to be smooth, as no singularity is expected for the PFM, and the dendrite is expected to evolve continuously as time advances.

In this work, four QoIs are considered: (1) the perimeter of dendrite L_d, (2) the area of dendrite S_d, (3) the segregation of Cu at solid-liquid interface κ, and (4) the length of primary arm of dendrite P_d. Since the microstructure determines the final properties of products, it is important to quantify the morphology of the microstructure. Three QoIs including dendritic perimeter, dendritic area and primary arm length are good metrics to quantify the morphology of the microstructure. The segregation of Cu is used to quantify the microsegregation at the interface.

Dendrite growth are strongly related to the grain growth, as both are competitive in nature [73]. Bostanabad et al. [74], Liu et al. [75], Li [76], and Bargmann et al. [77] provided a comprehensive review for computational microstructure reconstruction, generation, and characterization techniques, with statistical and deterministic physics-based microstructure descriptors. Dendritic morphology is highly correlated to the final grain microstructure, e.g. grain area and grain aspect ratio. Thus, in the scope of this paper, three dendritic QoIs related to the grain size, namely the dendritic perimeter, the dendritic area, and the primary arm length, are considered.

4.2 Dendritic perimeter

The perimeter of the dendrite, denoted as L_d, is the first QoI. To compute the perimeter of the dendrite, the phase field composition is extracted after a number of time steps. Figure 3a and Figure 3b present the contours of the dendrite in Al-4wt%Cu binary alloy at different snapshots. The contours are highlighted around the solid dendrite. A threshold is imposed based on the phase field composition to convert the simulation outputs to gray scale images. Then, the contours are retrieved from the binary images using Suzuki algorithm [78]. The contour extraction is implemented based on the OpenCV toolkit [79].

(a) Dendrite contour at timestep 3000.

(b) Dendrite contour at timestep 6000.

Figure 3: Perimeter and area computation of the dendrite in Figure 2 via finding contour with image processing. Readers are referred to the online manuscript for color version. Green lines indicate the contours, whereas black region corresponds the Cu-rich region, and white region corresponds to the Al-rich region.

4.3 Dendritic area

The area of the dendrite, denoted as S_d, is the second QoI in this study. The computation of dendritic area is performed in a similar approach as the dendritic perimeter, in which a phase field contour is extracted based on the phase field composition function, as in Figure 3. After a non-self-intersecting contour of dendrite is extracted, the dendritic area is computed as the contour area through Green formula. The computation of dendritic area occurs after a fixed number of time steps, based on the frequency of phase field composition outputs of the PFM, and is implemented using the OpenCV toolkit similarly.

4.4 Cu segregation

In literature, the segregation coefficient is typically defined as the ratio between composition of solid and that of liquid. This definition holds for single-component materials systems. However, for multi-component materials systems. The definition of segregation coefficient must be defined based on one component. In this case, we define the segregation coefficient based on Cu.

The segregation of Cu at solid-liquid interface, denoted as κ, is used as the third QoI, and calculated as

$$\kappa = \frac{C_l^i}{C_s^i} \tag{18}$$

where C_l^i and C_s^i are the compositions of liquid and solid phase at the interface, respectively. The deviation of the segregation coefficient κ from one determines the amount of actual segregation. Notice that the segregation of Cu at the interface κ is different from the partition coefficient k. The computation of Cu segregation quantity occurs after a fixed number of time steps, based on the phase field composition outputs of the PFM. It has been shown that high Cu segregation indicator κ promotes the Al_2Cu θ intermetallic phase [80] on the grain boundary or inside the grain. The Al_2Cu θ phase is associated with a higher mechanical strength of the material. Thus, κ serves as an implicit link between structure and property relationship.

4.5 Dendritic primary arm length

The dendritic primary arm length, denoted as P_d, is the fourth QoI. Based on the extracted spatial phase field composition from the PFM simulation, the dendritic primary arm length is computed

based on the locations of the pixels where Cu-rich phase switches to Al-rich phase along $< 1, 0, 0 >$ and $< 0, 1, 0 >$ crystallographic directions.

4.6 Mesh convergence study

In order to assess the sensitivity and numerical stability of the implemented PFM, a mesh convergence study is conducted to ensure that the QoIs do not drastically change with respect to the spatio-temporal discretization scheme. Figure 4a presents four QoIs along time steps, where independent runs with different time steps have been performed and post-processed. It is seen that the chosen time step of $2.0 \cdot 10^{-5} s$ is stable for all four QoIs. Figure 4b to Figure 4f presents a qualitative analysis of dendrites using different mesh sizes, 300×300, 400×400, 600×600, and 750×750, also showing a numerical stability of QoIs at the chosen mesh size of 300×300. von Neumann stability is taken into account to reduce the time-step accordingly, corresponding to the increase in the mesh size.

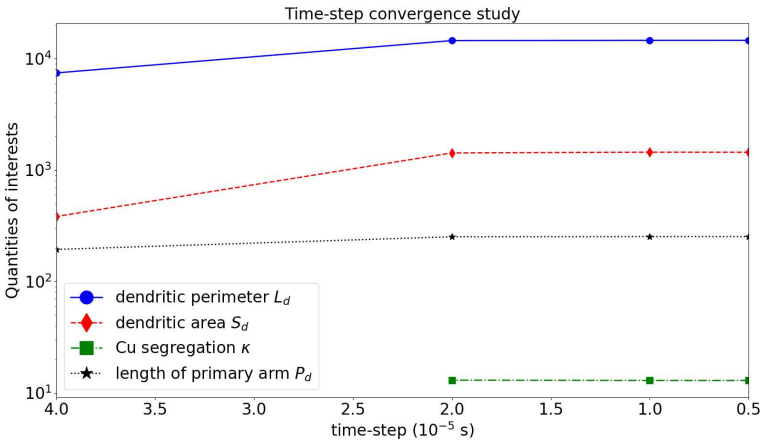

(a) Time-step convergence analysis.

(b) 750 (c) 600 (d) 500 (e) 400 (f) 300

Figure 4: Mesh-timestep convergence study.

5 Numerical Results

In Section 5.1, the QoIs are regarded as functions of process parameters at some fixed values of thermodynamic parameters, and vice versa. The SG method is employed to expand the QoIs through high-dimensional interpolation of the input parameters.

In Section 5.2, the PDFs of the QoIs are estimated based on the assumption that the thermodynamic parameters ($\sigma_0^*, \varepsilon^*$ and M_{phi}) are uniformly distributed between the lower and upper bounds in Table 2. The process parameters, on the other hand, are assumed to be fixed and known. The PDFs of the QoIs for different fixed values of process parameters are computed numerically.

5.1 QoIs as functions of process and thermodynamic parameters

Figure 5 shows dendritic morphology variations on SG nodes, as functions of process parameters. Both high cooling rate and low initial temperature promote the overall dendritic growth and the growth of the secondary dendritic arms. This is because that higher cooling rate and lower initial temperature result in higher driving force, which promotes the dendritic growth. Meanwhile, faster dendritic growth causes a higher segregation of Cu at the solid-liquid interface because there is less time for the solute Cu at the interface to diffuse. The initial temperature seems to have a larger impact on the secondary arm length than the cooling rate. At $T_0 = 915K$, the secondary arms grow more densely, compared to those at $T_0 = 920K$. To be representative, the dendrite at each node is fixed at a nominal thermodynamic parameter value.

Figure 6 shows the contour map of four different QoIs as functions of process parameters. The corresponding dendritic morphology on SG is shown in Figure 5. The dendritic morphology changes dramatically with respect to the initial temperature. A lower initial temperature causes a higher undercooling and driving force, which encourages the dendritic growth. The low initial temperature promotes the dendritic growth in all aspects, particularly the dendrite secondary arm growth. The secondary arm counts, as well as the dendritic area and perimeter are monotonic in the chosen bound of the initial temperature $[915, 920]K$. The cooling rate also has an effect on the dendritic growth. However, qualitatively, the dendritic morphology does not change significantly with respect to the cooling rate in the chosen bound [-20,-10] K/s, as shown in Figure 5. Quantitatively, higher cooling rate promotes dendritic growth, as manifested by the dendritic area and dendritic perimeter,

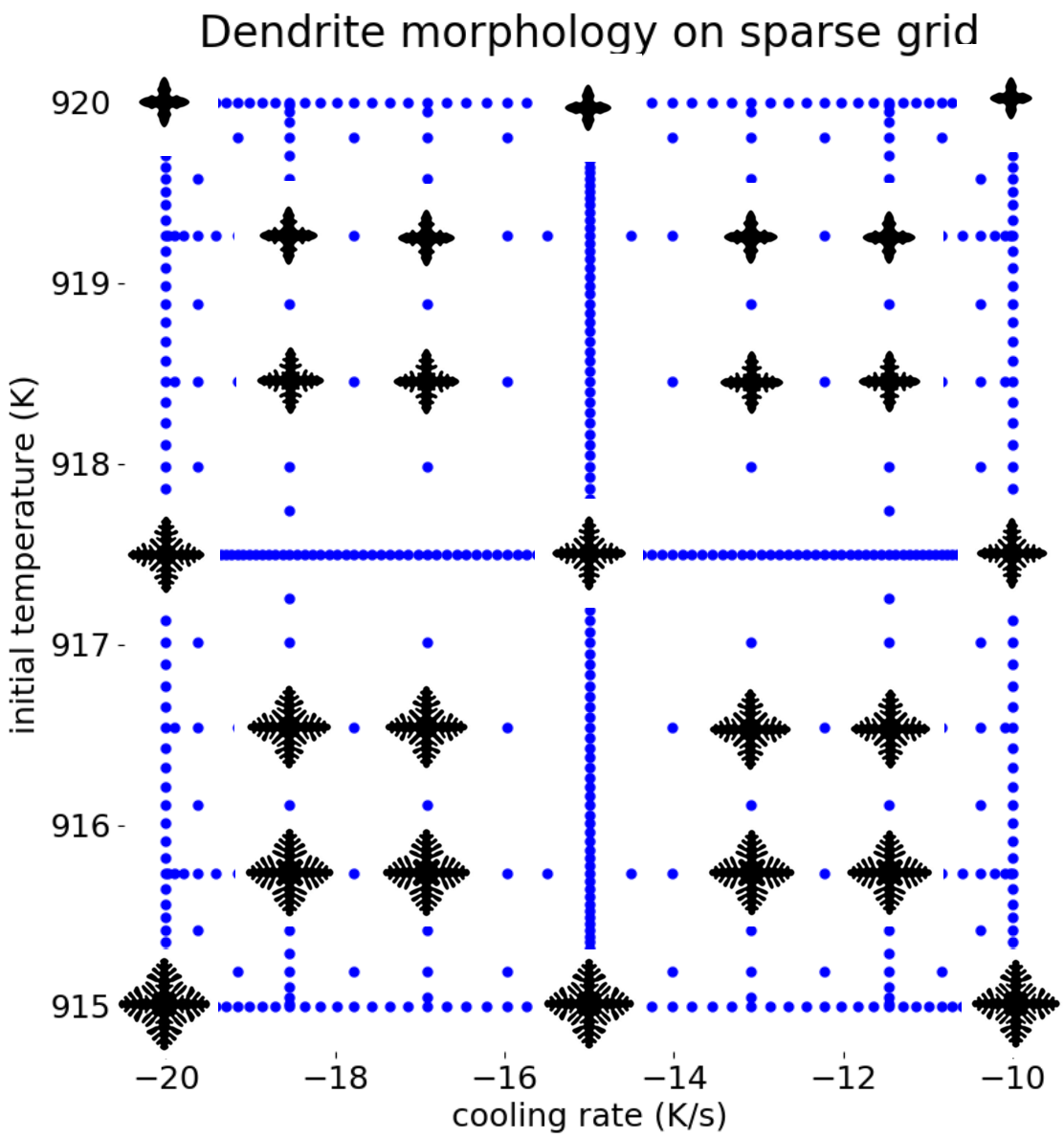

Figure 5: Representative dendritic morphology on SG as process parameters vary, i.e. cooling rate and initial temperature. The thermodynamic parameters are fixed at $\varepsilon^* = 0.35, \sigma_0^* = 0.24, M_\phi = 4 \cdot 10^{-9}$, respectively.

as shown in Figure 6. However, the initial temperature appears to play a major role in promoting dendritic growth, as well as morphing the dendrite. Dendrites with more secondary arms have larger areas and perimeters.

Cu segregation κ is a monotonic function of process parameters, including cooling rate $\frac{\partial T}{\partial t}$ and the initial temperature T_0, in the range of study, as shown in Figure 6c. Particularly, the Cu segregation κ increases with respect to a faster cooling rate and lower initial temperature. The initial temperature T_0 has a dominant effect on the Cu segregation κ in the range used. The primary arm length P_d, as shown in Figure 6d, is a highly nonlinear function of the process parameters, but appears to be correlated with the initial temperature T_0 as well. Lower initial temperature T_0 tends to be weakly associated with higher primary dendritic arm length P_d.

Figure 7 shows the dendritic morphology variation with respect to the thermodynamic parameters, i.e. interface anisotropy ε^* and interface mobility M_ϕ. Because interface anisotropy ε^* models the difference between the primary and secondary growth directions of dendrites, it has a larger effect on the shape of dendrite than the dendritic growth speed. Therefore, interface anisotropy ε^* does not affect the dendritic growth speed much. Since the interface mobility M_ϕ is the constant ratio between dendritic growth velocity and driving force, a higher interface mobility results in faster dendritic growth. The dendritic morphology varies significantly with respect to the interface mobility M_ϕ. Higher interface mobility M_ϕ promotes the growth of dendrite secondary arms, and consequently, the dendritic area and the dendritic perimeter. It is noted that there is a small difference between Figure 7 and Figure 5 at the center of the dendrites. Particularly, the center of the dendrites in Figure 5 is more developed than the center of the dendrites in Figure 7. The center of the dendrites has an impact on the dendritic area and dendritic perimeter. If the center of the dendrites is well-developed, with substantial secondary arm growth, then the dendritic perimeter and dendritic area increase. If the center of the dendrites is under-developed, then the dendritic area and dendritic perimeter decrease.

It is observed that the dendritic area S_d and the dendritic perimeter P_d significantly increase when the interface mobility M_ϕ increases. This is because a higher interface mobility results in a higher growth speed of dendrite. When the initial temperature is low (915K), the dendritic area and perimeter are positively correlated with the interfacial energy stiffness. When the initial temperature is high (920K), which means the undercooling is low, the change of interfacial energy stiffness has a

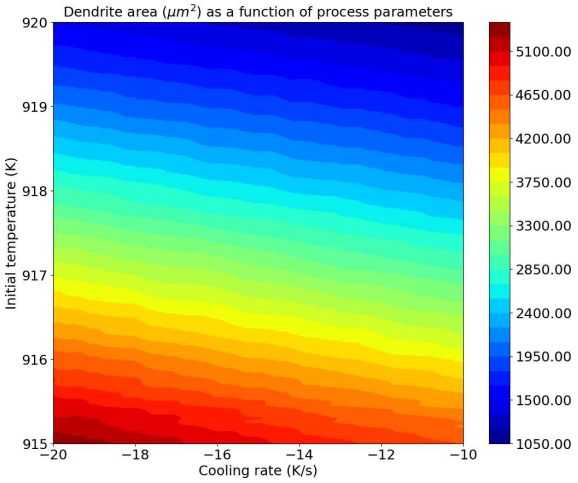

(a) Dendritic area $(\mu m)^2$ as a function of process parameters.

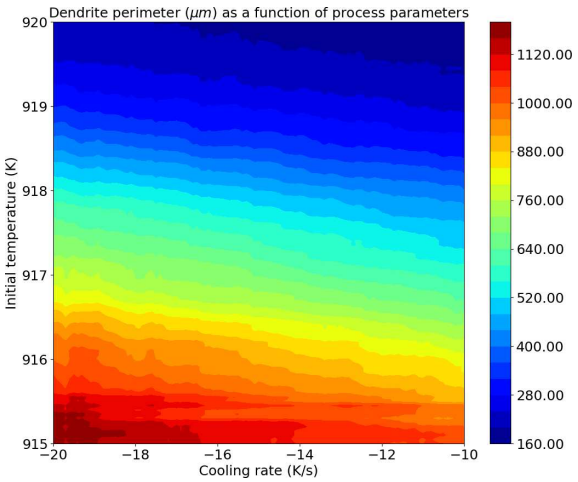

(b) Dendritic perimeter (μm) as a function of process parameters.

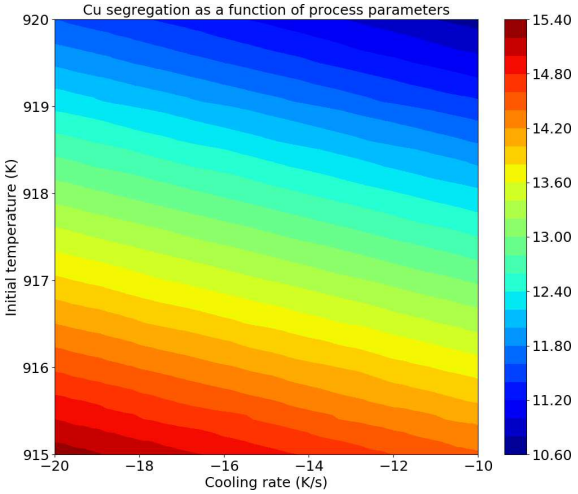

(c) Cu segregation as a function of process parameters.

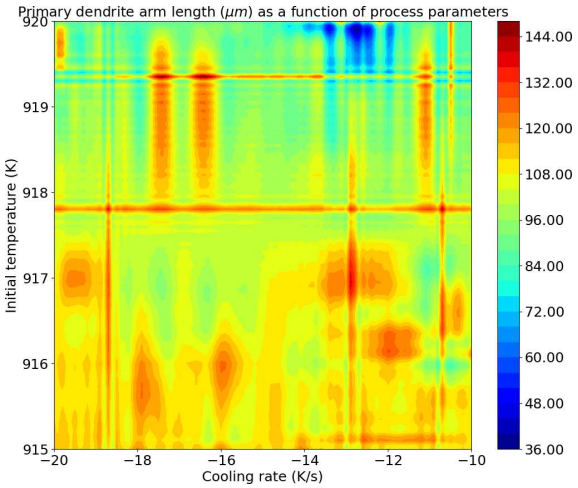

(d) Dendritic primary arm length (μm) as a function of process parameters.

Figure 6: Dendrite QoIs as functions of process parameters. Other thermodynamic parameters are fixed at $\varepsilon^* = 0.35, \sigma_0^* = 0.24, M_\phi = 4 \cdot 10^{-9}$, respectively.

trivial effect on the dendritic area and perimeter. The interface anisotropy ε^* does not change the dendritic area S_d and the dendritic perimeter P_d much. Qualitatively, the interface anisotropic ε^* parameter does not have a significant impact on the dendritic morphology. Quantitatively, as shown in Figure 8, the dendritic area and dendritic perimeter is sensitively dependent on the interface mobility M_ϕ. A small increase of M_ϕ substantially promotes the dendritic growth.

As illustrated in Figure 8c, the Cu segregation κ generally increases as the interface mobility M_ϕ increases. The relationship between κ and M_ϕ is not strictly monotonic. However, when Figure 8c and Figure 6c are compared, it is seen that the process parameters have stronger effects on the magnitude of Cu segregation than the thermodynamic parameters. The variation bound for κ in Figure 6c is [10.60,15.40], compared to [12.74,13.28] in Figure 8c.

The dendritic primary arm length P_d is shown to be a nonlinear function of thermodynamic parameters, as in Figure 8d. However, the variation is fairly mild, as most of the dendrites achieve roughly the same tip location with different thermodynamic parameters. There is a weak positive correlation between the interface mobility M_ϕ and the dendritic primary arm length P_d.

To further visualize the effect of all process and thermodynamic parameters on the dendrite, 3D contours of all QoIs, i.e. the dendritic area, dendritic perimeter, Cu segregation, and dendritic primary arm length, are plotted in Figure 9, Figure 10, Figure 11, and Figure 12, respectively. The process parameters are further divided into subplot of each figure, where the cooling rate $\dfrac{\partial T}{\partial t}$ and the initial temperature T_0 are fixed at four corners of the SG, corresponding to the lower and upper bounds of each parameters. The QoIs are then plotted as functions of three thermodynamic parameters, i.e. prefactor of interfacial energy stiffness σ_0^*, interface anisotropy ε^*, and interface mobility M_ϕ, using 3D contour plots.

Figure 9 shows the dendritic area variation as a function of thermodynamic parameters. Initial temperature T_0 plays a major role in dendritic growth, as slightly lower temperature significantly accelerates dendritic area. An increase in interface mobility M_ϕ corresponds to an increase in dendritic area. Figure 10 shows the dendritic perimeter variations as a function of input parameters. The dendritic area and dendritic perimeter are highly correlated, as shown in Figure 9 and Figure 10. Figure 11 plots the Cu segregation κ, showing a mild variation with respect to thermodynamic parameters. Namely, lower interface anisotropy ε^* and higher interface mobility M_ϕ generally result in higher κ. However, as shown previously in Figure 6c, the Cu segregation κ is more sensitive to

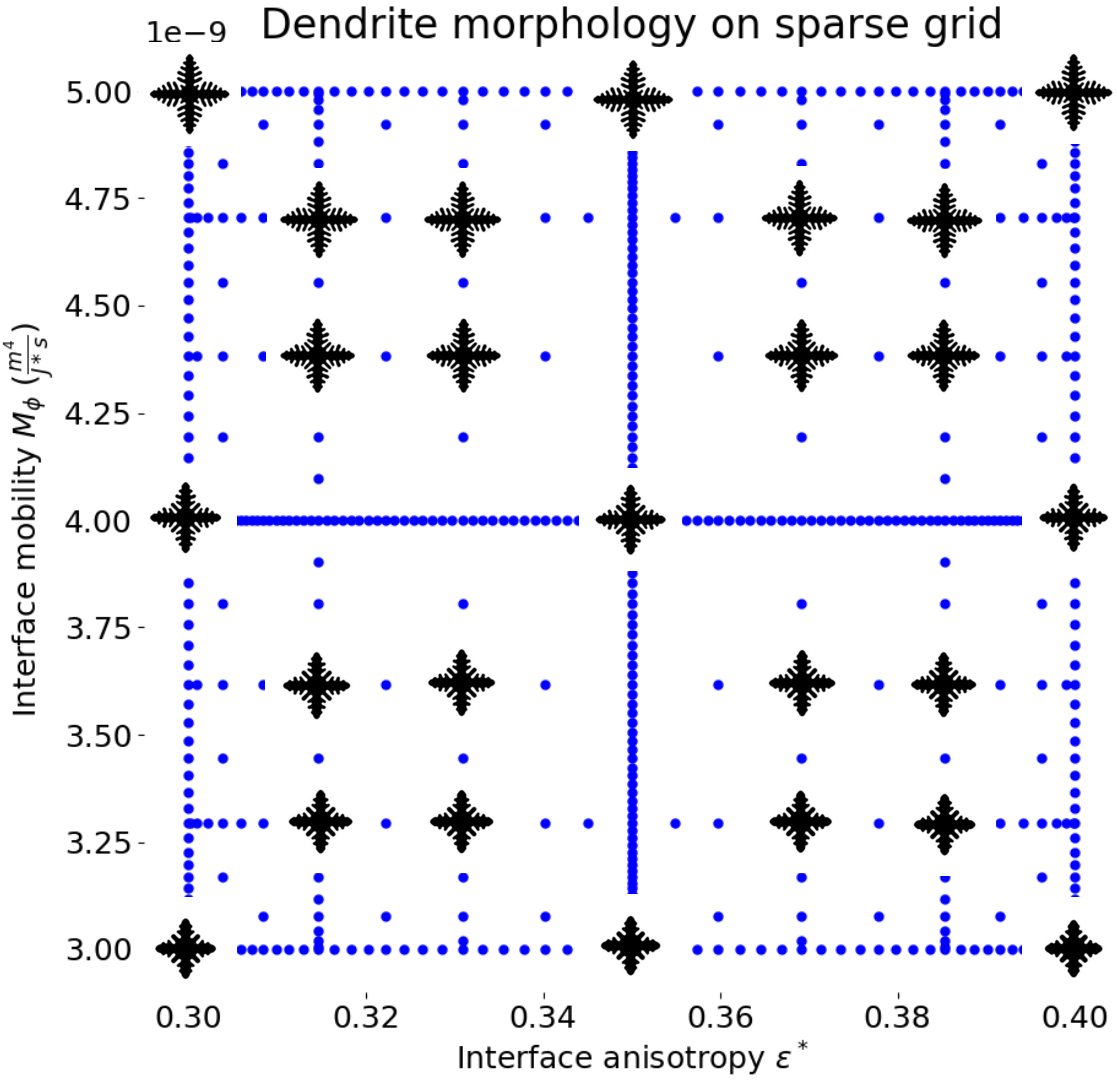

Figure 7: Dendritic morphology at different thermodynamic parameters on SG, where other parameters are fixed at $\frac{\partial T}{\partial t} = -15K/s$, $T_0 = 917.5$, and $\sigma_0^* = 0.24$.

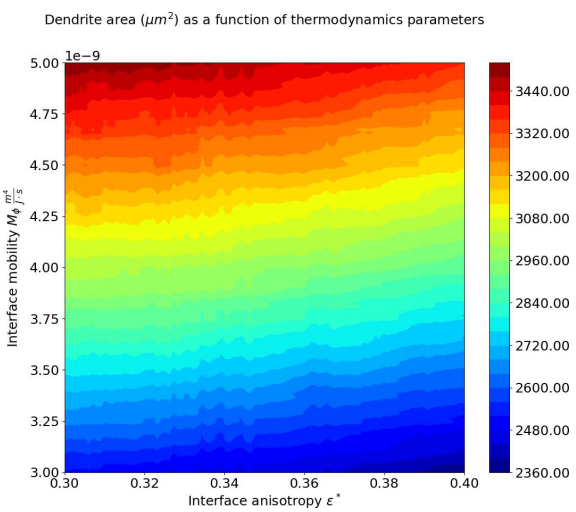

(a) Dendritic area $(\mu m)^2$ as a function of thermodynamic parameters.

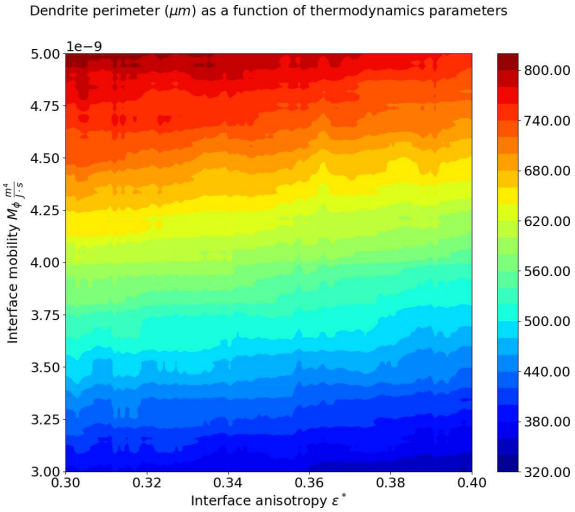

(b) Dendritic perimeter (μm) as a function of thermodynamic parameters.

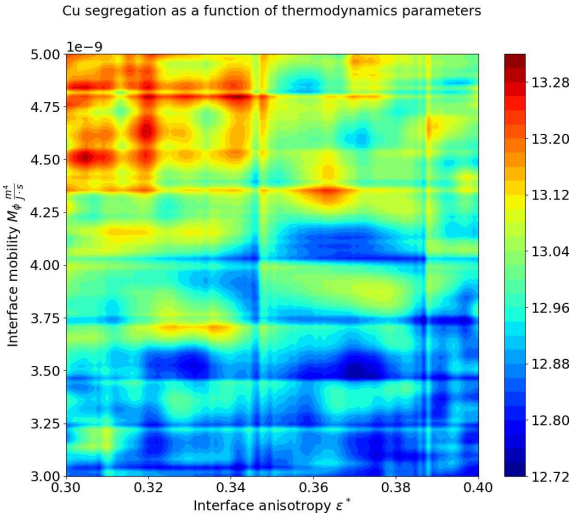

(c) Cu segregation as a function of thermodynamic parameters.

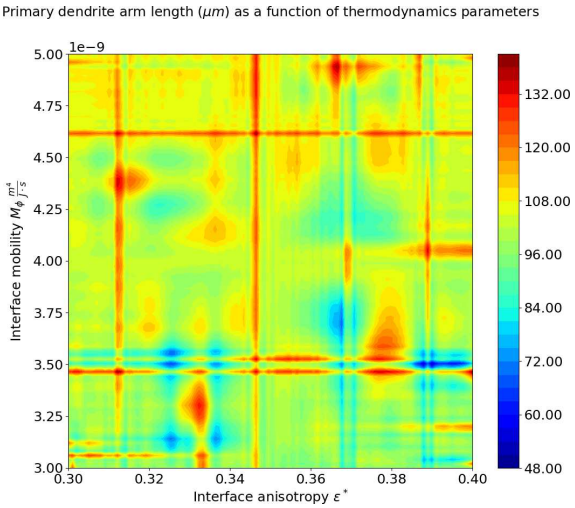

(d) Dendritic primary arm length (μm) as a function of thermodynamic parameters.

Figure 8: Dendrite QoIs as functions of thermodynamic parameters. Other process parameters are fixed at $\frac{\partial T}{\partial t} = -15K/s$, $T_0 = 917.5$, and $\sigma_0^* = 0.24$.

the initial temperature T_0, compared to other thermodynamic parameters. It has been shown that high κ promotes the θ phase Al_2C on the grain boundary or inside the grain, consequently resulting in a higher mechanical strength of material. Figure 12 presents the dendritic primary arm length, showing a mild dependence on the initial temperature T_0 and the interface mobility M_ϕ, as in Figure 6d and Figure 8d, respectively. Readers are referred to the online version of color plots.

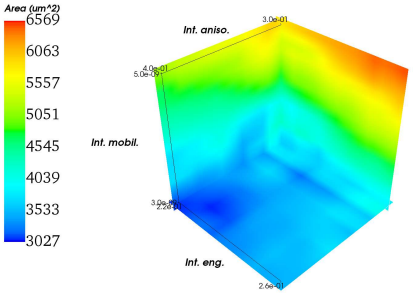

(a) Dendritic area as a function of thermodynamic parameters. Cooling rate $\frac{\partial T}{\partial t}$ and initial temperature T_0 are fixed at -10K/s and 915K, respectively.

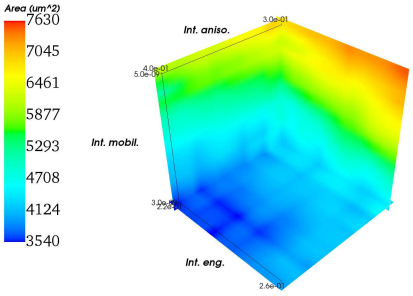

(b) Dendritic area as a function of thermodynamic parameters. Cooling rate $\frac{\partial T}{\partial t}$ and initial temperature T_0 are fixed at -20K/s and 915K, respectively.

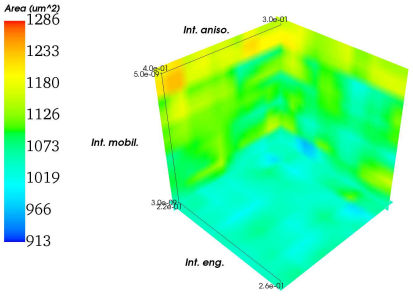

(c) Dendritic area as a function of thermodynamic parameters. Cooling rate $\frac{\partial T}{\partial t}$ and initial temperature T_0 are fixed at -10K/s and 920K, respectively.

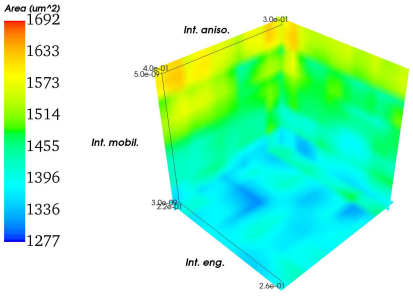

(d) Dendritic area as a function of thermodynamic parameters. Cooling rate $\frac{\partial T}{\partial t}$ and initial temperature T_0 are fixed at -20K/s and 920K, respectively.

Figure 9: 3D contours of dendritic area as a function of thermodynamic parameters, with different fixed values of process parameters.

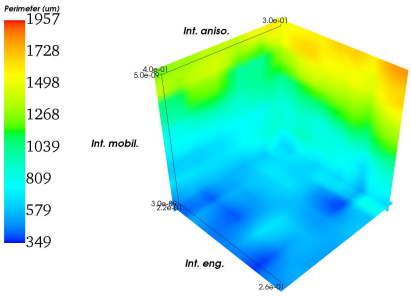

(a) Dendritic perimeter as a function of thermodynamic parameters. Cooling rate $\frac{\partial T}{\partial t}$ and initial temperature T_0 are fixed at -10K/s and 915K, respectively.

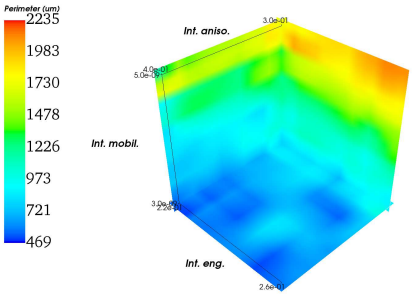

(b) Dendritic perimeter as a function of thermodynamic parameters. Cooling rate $\frac{\partial T}{\partial t}$ and initial temperature T_0 are fixed at -20K/s and 915K, respectively.

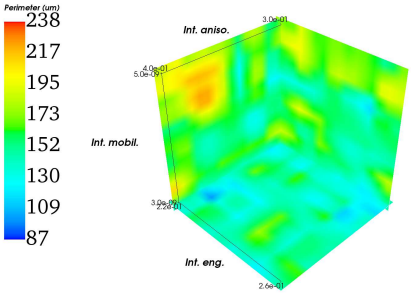

(c) Dendritic perimeter as a function of thermodynamic parameters. Cooling rate $\frac{\partial T}{\partial t}$ and initial temperature T_0 are fixed at -10K/s and 920K, respectively.

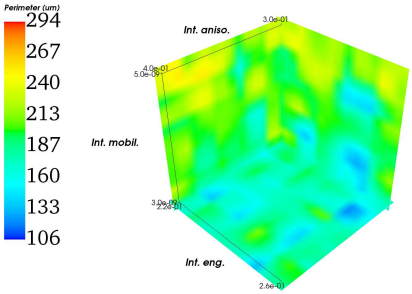

(d) Dendritic perimeter as a function of thermodynamic parameters. Cooling rate $\frac{\partial T}{\partial t}$ and initial temperature T_0 are fixed at -20K/s and 920K, respectively.

Figure 10: 3D contours of dendrite parameter as a function of thermodynamic parameters, with different fixed values of process parameters.

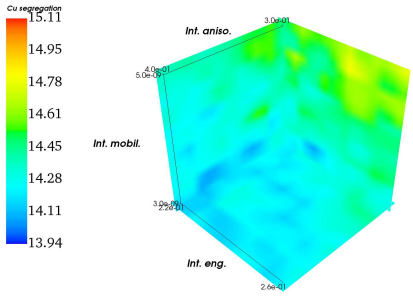

(a) Cu segregation as a function of thermodynamic parameters. Cooling rate $\frac{\partial T}{\partial t}$ and initial temperature T_0 are fixed at -10K/s and 915K, respectively.

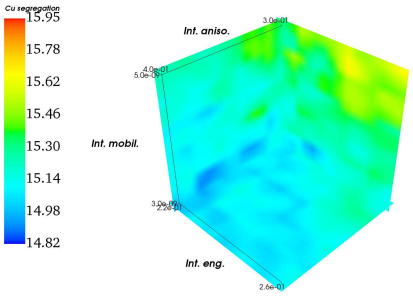

(b) Cu segregation as a function of thermodynamic parameters. Cooling rate $\frac{\partial T}{\partial t}$ and initial temperature T_0 are fixed at -20K/s and 915K, respectively.

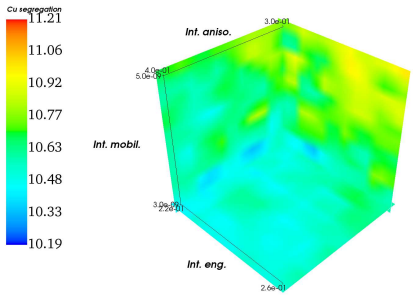

(c) Cu segregation as a function of thermodynamic parameters. Cooling rate $\frac{\partial T}{\partial t}$ and initial temperature T_0 are fixed at -10K/s and 920K, respectively.

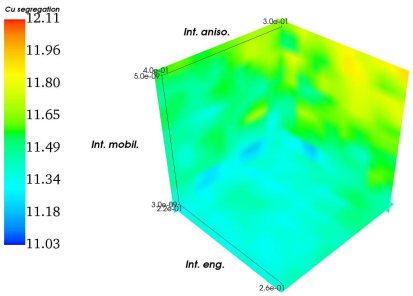

(d) Cu segregation as a function of thermodynamic parameters. Cooling rate $\frac{\partial T}{\partial t}$ and initial temperature T_0 are fixed at -20K/s and 920K, respectively.

Figure 11: 3D contours of Cu segregation as a function of thermodynamic parameters, with different fixed values of process parameters.

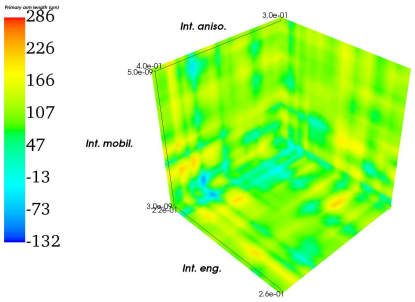

(a) Dendritic primary arm length as a function of thermodynamic parameters. Cooling rate $\frac{\partial T}{\partial t}$ and initial temperature T_0 are fixed at -10K/s and 915K, respectively.

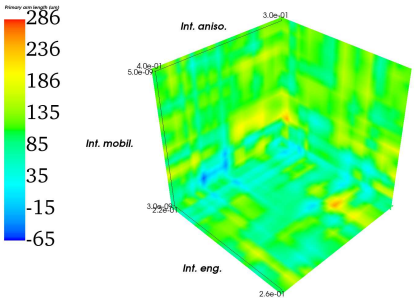

(b) Dendritic primary arm length as a function of thermodynamic parameters. Cooling rate $\frac{\partial T}{\partial t}$ and initial temperature T_0 are fixed at -20K/s and 915K, respectively.

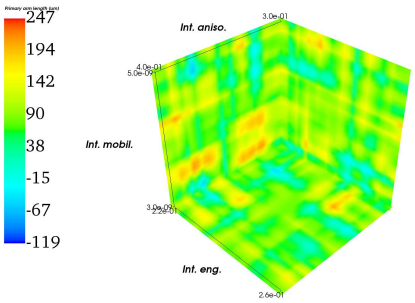

(c) Dendritic primary arm length as a function of thermodynamic parameters. Cooling rate $\frac{\partial T}{\partial t}$ and initial temperature T_0 are fixed at -10K/s and 920K, respectively.

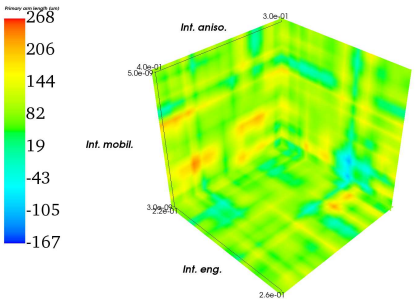

(d) Dendritic primary arm length as a function of thermodynamic parameters. Cooling rate $\frac{\partial T}{\partial t}$ and initial temperature T_0 are fixed at -20K/s and 920K, respectively.

Figure 12: 3D contours of dendritic primary arm length as a function of thermodynamic parameters, with different fixed values of process parameters.

5.2 PDFs and statistics of the QoIs with respect to random thermodynamic parameters

In this section, non-intrusive spectral projection is applied to compute the PCE coefficients and the distribution of the QoIs. The process parameters, T_0 and $\frac{\partial T}{\partial t}$, are set to be fixed assuming that those variables are controllable in practice. The thermodynamic parameters, σ_0^*, ε^*, and M_ϕ, however, are assumed to be random, and uniformly distributed between the lower and upper bounds according to Table 3.

UQToolKit [81, 82] is utilized to calculate PCE coefficients, which are obtained by Galerkin projection in theory. Orthogonal Legendre polynomials of the sixth order are used in constructing the PDFs of the QoIs. A two-dimensional SG is constructed for process parameters. A PDF is constructed at each node of the SG. The mean and standard deviation are then calculated for each node, i.e. each fixed couple of values of process parameters. These quantities are then reconstructed on the whole two-dimensional process parameter space using SG formulation.

Figures 13a, 13b, 13c, and 13d show the PDFs of the dendritic area, dendritic perimeter, Cu segregation, and the dendritic arm length, respectively, where the thermodynamic parameters in Table 3, namely σ_0^*, ε^*, and M_ϕ are considered to be uniformly distributed between the lower and upper bounds. Several observations are made. First, the dendritic area and perimeter are highly correlated. Second, as shown in Figure 13a and Figure 13b, the initial temperature T_0 is the dominant factor for the dendritic growth in terms of size, that decreasing the initial temperature T_0 corresponding to larger dendrite size. The cooling rate $\frac{\partial T}{\partial t}$ also affects the dendrite size, but is a less dominant factor. The same observation can be made for the Cu segregation κ, as shown in Figure 13c. It is also observed that the standard deviation of the Cu segregation κ only changes mildly, with different process parameters, as opposed to substantial changes in the standard deviations of dendritic area and dendritic perimeter. The dendritic primary arm length is more unpredictable, as shown in Figure 13d, where the mean deviates slightly around $100\mu m$. The observations are consistent with the previous observation in Section 5.1.

Figure 14 and Figure 15 show the prediction map of the mean and standard deviation, respectively. The predicted mean is similar to the prediction shown in Figure 6. Figure 15 indicates that there is a weak correlation between the statistical standard deviation and the statistical mean for the first three QoIs, namely the dendritic area, the dendritic perimeter, and the Cu segregation.

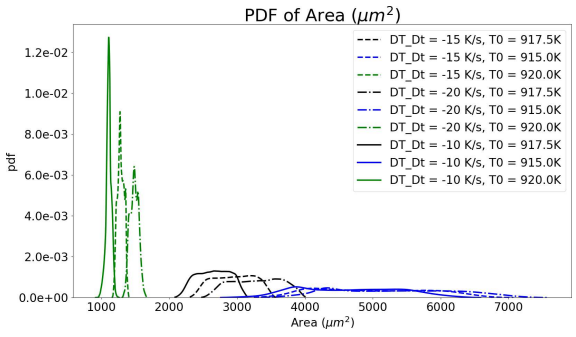

(a) PDF of dendritic area (μm^2).

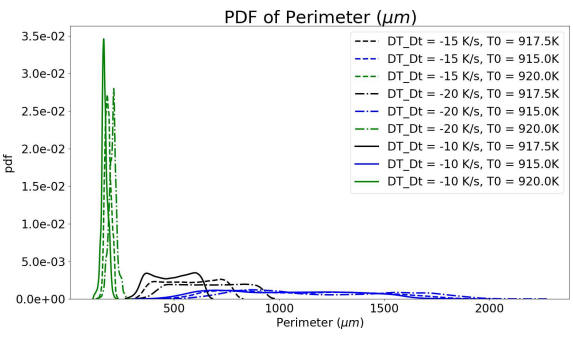

(b) PDF of dendritic perimeter (μm).

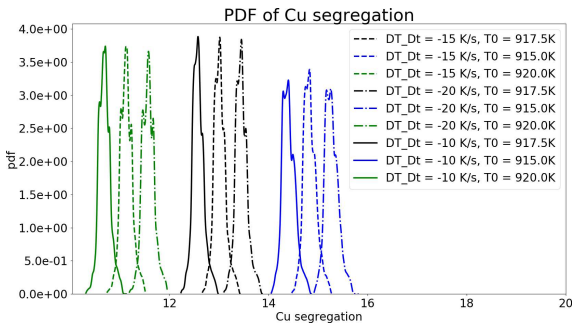

(c) PDF of Cu segregation.

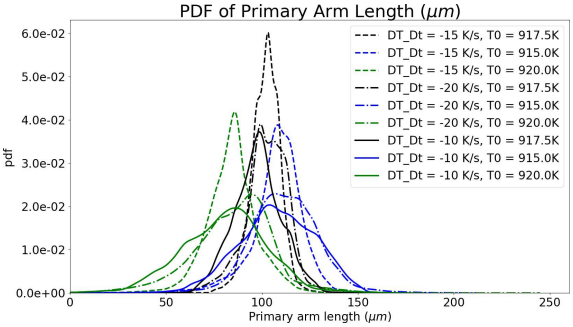

(d) PDF of dendritic primary arm length.

Figure 13: Probability density function of QoIs at different process parameters, where the thermodynamic parameters are distributed uniformly between the lower and upper bounds in Table 3.

The dendritic primary arm length appears to be a nonlinear function, and weakly dependent on the initial temperature.

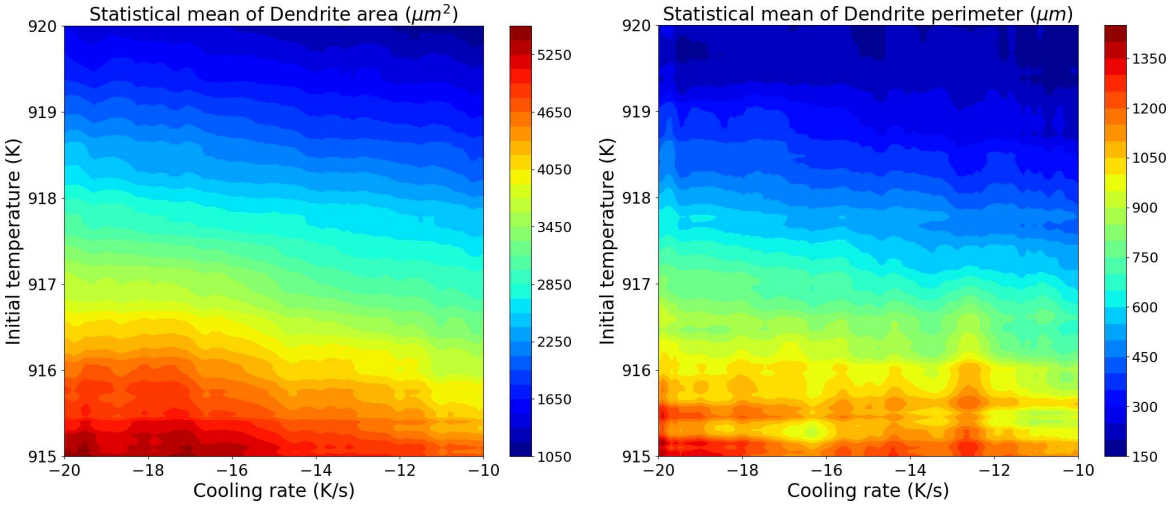

(a) Mean of dendritic area (μm^2).

(b) Mean of dendritic perimeter (μm).

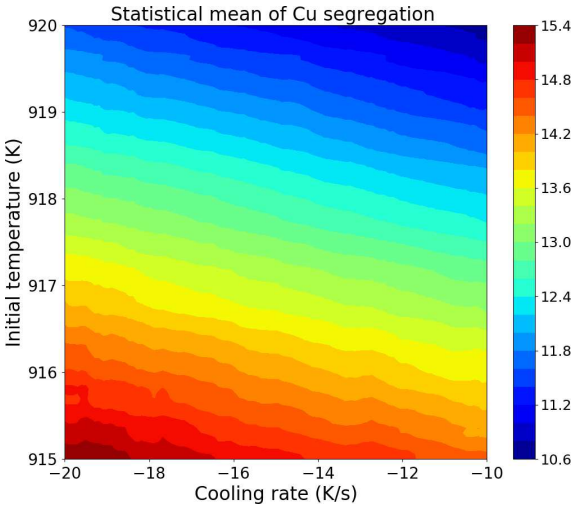

(c) Mean of Cu segregation.

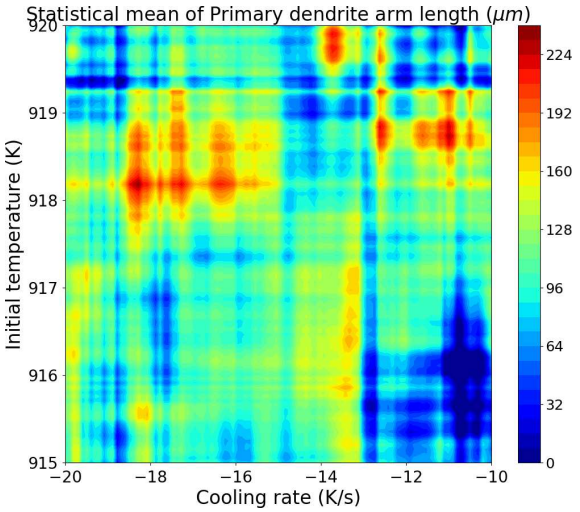

(d) Mean of dendritic primary arm length.

Figure 14: Statistical means of the QoIs, where PDFs are shown in Figure 13.

6 Discussion

In this study, we investigate the dendrite properties with respect to thermodynamic and process parameters. While process parameters can be controlled, the thermodynamic parameters are materials

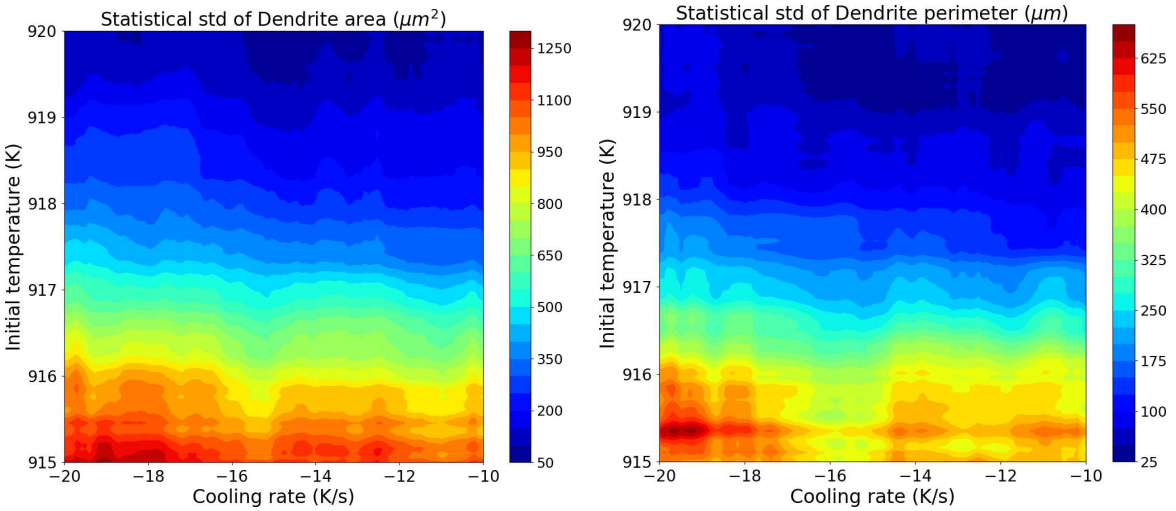

(a) Std of dendritic area (μm^2).

(b) Std of dendritic perimeter (μm).

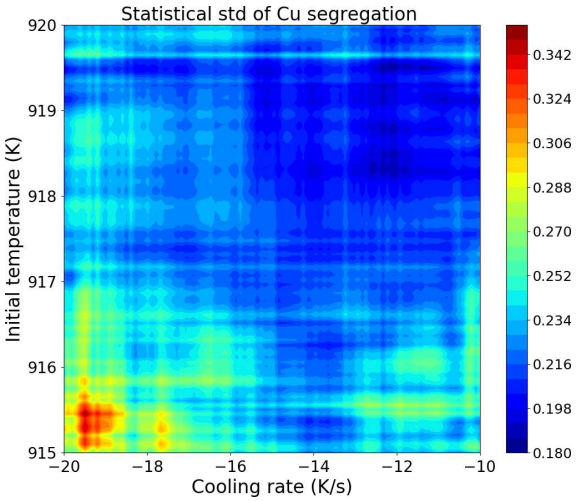

(c) Std of Cu segregation.

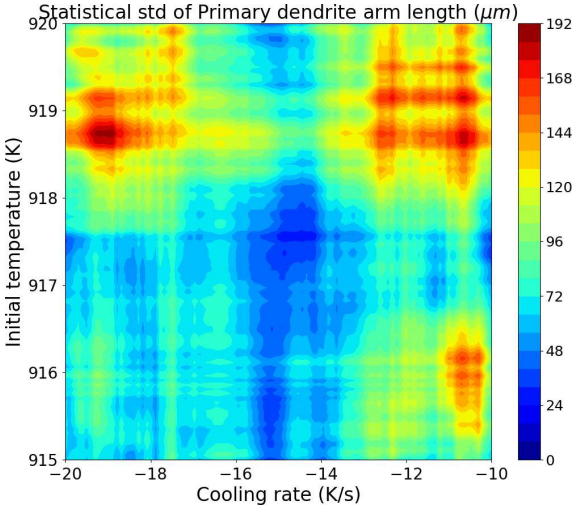

(d) Std of dendritic primary arm length.

Figure 15: Standard deviations (std's) of the QoIs, where PDFs are shown in Figure 13.

properties and cannot be controlled, but can be quantified with certain variation ranges. Different thermodynamic parameters result in different dendritic morphology and properties.

The variation of dendrite properties with respect to the thermodynamic parameters can be used as a guide for thermodynamic parameters calibration. Qualitative analysis includes comparison between experimental and simulated dendritic morphology, and rough estimation of dendrite size with respect to solidification time. The dendrite shape can also be quantitatively measured by shape descriptors, which are extracted via image processing techniques. Figure 16 presents the shape analysis based on the medial axis method. The extracted skeleton contains shape information, which can be used for shape matching. However, one of the main challenges in shape matching is the inherent randomness in composition and interface distributions.

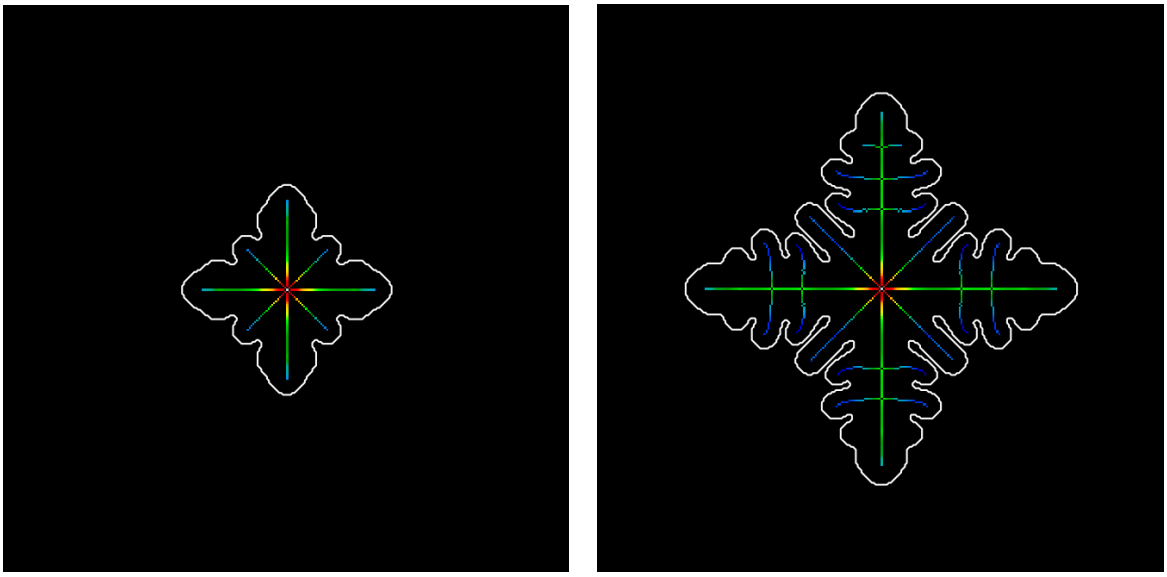

(a) Dendrite skeleton at timestep 3000.

(b) Dendrite skeleton at timestep 6000.

Figure 16: Skeletonization of the dendrite in Figure 3 at different snapshots.

The process parameters are typically controlled during the manufacturing process, where sensors can be embedded and controllers are activated. However, fluctuation still exists for controllable process parameters, which leads to imperfect control conditions.

7 Conclusion

In this work, the effects of parameter uncertainty on the PFM prediction of process-structure relationships in alloy solidification are investigated. Five input parameters for PFM simulations are included, two of which are process parameters, and the other three are thermodynamic parameters. Image processing techniques are utilized to extract structural descriptors analyze the dendritic morphology quantitatively. The UQ study is conducted based on SG with a high-dimensional interpolation framework. 19313 PFM simulations are performed with different input parameters, where the bounds are chosen *a priori*. It is shown that the count of secondary arm necessarily correlates with the dendritic area and dendritic perimeter. The dendritic area is positively correlated with the dendritic perimeter, i.e. dendrite with larger area also has a longer perimeter. The UQ study aims to establish the structure-property relationship between the dendritic morphology and the high-dimensional process and thermodynamic input parameter space. The variation of dendrite properties has also been explored, in which thermodynamic parameters play a major role. Both process and thermodynamic parameters are shown to affect the dendritic growth, resulting in different microstructure, and thus different materials properties.

8 Acknowledgment

The research is supported in part by the National Science Foundation under grant number CMMI-1306996. HT acknowledges supports by U.S. Department of Energy through FASTMath SciDAC institute. The authors are thankful to anonymous reviewers for the comments to improve the manuscript.

References

[1] D. Liu and Y. Wang, "Mesoscale multi-physics simulation of rapid solidification of Ti-6Al-4V alloy," *Additive Manufacturing*, vol. 25, pp. 551–562, 2019.

[2] A. Chernatynskiy, S. R. Phillpot, and R. LeSar, "Uncertainty quantification in multiscale simulation of materials: A prospective," *Annual Review of Materials Research*, vol. 43, pp. 157–182, 2013.

[3] Y. Wang, "Uncertainty in materials modeling, simulation, and development for ICME," in *Proc. 2015 Materials Science and Technology*, 2015.

[4] Y. Wang and L. Swiler, "Special issue on uncertainty quantification in multiscale system design and simulation," *ASCE-ASME Journal of Risk and Uncertainty in Engineering Systems, Part B: Mechanical Engineering*, vol. 4, no. 1, p. 010301, 2018.

[5] K. Lejaeghere, V. Van Speybroeck, G. Van Oost, and S. Cottenier, "Error estimates for solid-state density-functional theory predictions: an overview by means of the ground-state elemental crystals," *Critical Reviews in Solid State and Materials Sciences*, vol. 39, no. 1, pp. 1–24, 2014.

[6] P. Pernot, B. Civalleri, D. Presti, and A. Savin, "Prediction uncertainty of density functional approximations for properties of crystals with cubic symmetry," *The Journal of Physical Chemistry A*, vol. 119, no. 21, pp. 5288–5304, 2015.

[7] J. J. Mortensen, K. Kaasbjerg, S. L. Frederiksen, J. K. Nørskov, J. P. Sethna, and K. W. Jacobsen, "Bayesian error estimation in density-functional theory," *Physical review letters*, vol. 95, no. 21, p. 216401, 2005.

[8] F. Hanke, "Sensitivity analysis and uncertainty calculation for dispersion corrected density functional theory," *Journal of computational chemistry*, vol. 32, no. 7, pp. 1424–1430, 2011.

[9] L. He and Y. Wang, "An efficient saddle point search method using kriging metamodels," in *ASME 2015 International Design Engineering Technical Conferences and Computers and Information in Engineering Conference*, pp. V01AT02A008–V01AT02A008, American Society of Mechanical Engineers, 2015.

[10] A. Tran, L. He, and Y. Wang, "An efficient first-principles saddle point searching method based on distributed kriging metamodels," *ASCE-ASME Journal of Risk and Uncertainty in Engineering Systems, Part B: Mechanical Engineering*, vol. 4, no. 1, p. 011006, 2018.

[11] F. Rizzi, H. Najm, B. Debusschere, K. Sargsyan, M. Salloum, H. Adalsteinsson, and O. Knio, "Uncertainty quantification in MD simulations. part I: Forward propagation," *Multiscale Modeling & Simulation*, vol. 10, no. 4, p. 1428, 2012.

[12] L. C. Jacobson, R. M. Kirby, and V. Molinero, "How short is too short for the interactions of a water potential? Exploring the parameter space of a coarse-grained water model using uncertainty quantification," *The Journal of Physical Chemistry B*, vol. 118, no. 28, pp. 8190–8202, 2014.

[13] P. N. Patrone, A. Dienstfrey, A. R. Browning, S. Tucker, and S. Christensen, "Uncertainty quantification in molecular dynamics studies of the glass transition temperature," *Polymer*, vol. 87, pp. 246–259, 2016.

[14] S. L. Frederiksen, K. W. Jacobsen, K. S. Brown, and J. P. Sethna, "Bayesian ensemble approach to error estimation of interatomic potentials," *Physical Review Letters*, vol. 93, no. 16, p. 165501, 2004.

[15] F. Cailliez and P. Pernot, "Statistical approaches to forcefield calibration and prediction uncertainty in molecular simulation," *The Journal of Chemical Physics*, vol. 134, no. 5, p. 054124, 2011.

[16] F. Rizzi, H. Najm, B. Debusschere, K. Sargsyan, M. Salloum, H. Adalsteinsson, and O. Knio, "Uncertainty quantification in MD simulations. part II: Bayesian inference of force-field parameters," *Multiscale Modeling & Simulation*, vol. 10, no. 4, p. 1460, 2012.

[17] P. Angelikopoulos, C. Papadimitriou, and P. Koumoutsakos, "Data driven, predictive molecular dynamics for nanoscale flow simulations under uncertainty," *The Journal of Physical Chemistry B*, vol. 117, no. 47, pp. 14808–14816, 2013.

[18] G. Dhaliwal, P. B. Nair, and C. V. Singh, "Uncertainty analysis and estimation of robust AIREBO parameters for graphene," *Carbon*, 2018.

[19] A. Tran and Y. Wang, "A molecular dynamics simulation mechanism with imprecise interatomic potentials," in *Proceedings of the 3rd World Congress on Integrated Computational Materials Engineering (ICME)*, pp. 131–138, John Wiley & Sons, 2015.

[20] A. Tran and Y. Wang, "Reliable Molecular Dynamics: Uncertainty quantification using interval analysis in molecular dynamics simulation," *Computational Materials Science*, vol. 127, pp. 141–160, 2017.

[21] S. T. Reeve and A. Strachan, "Error correction in multi-fidelity molecular dynamics simulations using functional uncertainty quantification," *Journal of Computational Physics*, vol. 334, pp. 207–220, 2017.

[22] M. A. Tschopp, B. C. Rinderspacher, S. Nouranian, M. I. Baskes, S. R. Gwaltney, and M. F. Horstemeyer, "Quantifying parameter sensitivity and uncertainty for interatomic potential design: Application to saturated hydrocarbons," *ASCE-ASME Journal of Risk and Uncertainty in Engineering Systems, Part B: Mechanical Engineering*, vol. 4, no. 1, p. 011004, 2018.

[23] Y. Wang, "Reliable kinetic Monte Carlo simulation based on random set sampling," *Soft Computing*, vol. 17, no. 8, pp. 1439–1451, 2013.

[24] Y. Wang, "Multiscale uncertainty quantification based on a generalized hidden Markov model," *Journal of Mechanical Design*, vol. 133, no. 3, p. 031004, 2011.

[25] A. E. Tallman, L. P. Swiler, Y. Wang, and D. L. McDowell, "Reconciled top-down and bottom-up hierarchical multiscale calibration of bcc Fe crystal plasticity," *International Journal for Multiscale Computational Engineering*, vol. 15, no. 6, 2017.

[26] L. Bertini, S. Brassesco, and P. Buttà, "Front fluctuations for the stochastic Cahn–Hilliard equation," *Brazilian Journal of Probability and Statistics*, vol. 29, no. 2, pp. 336–371, 2015.

[27] T. Funaki, "Sharp interface limits for a stochastic Allen-Cahn equation," in *Lectures on Random Interfaces*, pp. 93–110, Springer, 2016.

[28] L. Bo, Y. Jiang, and Y. Wang, "Stochastic Cahn–Hilliard equation with fractional noise," *Stochastics and Dynamics*, vol. 8, no. 04, pp. 643–665, 2008.

[29] Y. Wang, "Model-form calibration in drift-diffusion simulation using fractional derivatives," *ASCE-ASME Journal of Risk and Uncertainty in Engineering Systems, Part B: Mechanical Engineering*, vol. 2, no. 3, p. 031006, 2016.

[30] A. Karma and W.-J. Rappel, "Quantitative phase-field modeling of dendritic growth in two and three dimensions," *Physical review E*, vol. 57, no. 4, p. 4323, 1998.

[31] M. A. Jaafar, D. R. Rousse, S. Gibout, and J.-P. Bédécarrats, "A review of dendritic growth during solidification: Mathematical modeling and numerical simulations," *Renewable and Sustainable Energy Reviews*, vol. 74, pp. 1064–1079, 2017.

[32] R. Sekerka, "A stability function for explicit evaluation of the Mullins-Sekerka interface stability criterion," *Journal of Applied Physics*, vol. 36, no. 1, pp. 264–268, 1965.

[33] M. E. Glicksman, *Principles of solidification: an introduction to modern casting and crystal growth concepts*. Springer Science & Business Media, 2010.

[34] A. Karma, "Phase-field formulation for quantitative modeling of alloy solidification," *Physical Review Letters*, vol. 87, no. 11, p. 115701, 2001.

[35] S. G. Kim, "A phase-field model with antitrapping current for multicomponent alloys with arbitrary thermodynamic properties," *Acta Materialia*, vol. 55, no. 13, pp. 4391–4399, 2007.

[36] J. Tiaden, B. Nestler, H.-J. Diepers, and I. Steinbach, "The multiphase-field model with an integrated concept for modelling solute diffusion," *Physica D: Nonlinear Phenomena*, vol. 115, no. 1-2, pp. 73–86, 1998.

[37] J. Eiken, B. Böttger, and I. Steinbach, "Multiphase-field approach for multicomponent alloys with extrapolation scheme for numerical application," *Physical Review E*, vol. 73, no. 6, p. 066122, 2006.

[38] W. W. Mullins and R. F. Sekerka, "Morphological stability of a particle growing by diffusion or heat flow," *Journal of applied physics*, vol. 34, no. 2, pp. 323–329, 1963.

[39] W. W. Mullins and R. Sekerka, "Stability of a planar interface during solidification of a dilute binary alloy," *Journal of applied physics*, vol. 35, no. 2, pp. 444–451, 1964.

[40] J. Langer, R. Sekerka, and T. Fujioka, "Evidence for a universal law of dendritic growth rates," *Journal of Crystal Growth*, vol. 44, no. 4, pp. 414–418, 1978.

[41] J. Langer and H. Müller-Krumbhaar, "Theory of dendritic growth—I. Elements of a stability analysis," *Acta Metallurgica*, vol. 26, no. 11, pp. 1681–1687, 1978.

[42] J. S. Langer, "Instabilities and pattern formation in crystal growth," *Reviews of Modern Physics*, vol. 52, no. 1, p. 1, 1980.

[43] H. Xing, X. Dong, J. Wang, and K. Jin, "Orientation dependence of columnar dendritic growth with sidebranching behaviors in directional solidification: insights from phase-field simulations," *Metallurgical and Materials Transactions B*, pp. 1–13, 2018.

[44] T. Takaki, R. Rojas, S. Sakane, M. Ohno, Y. Shibuta, T. Shimokawabe, and T. Aoki, "Phase-field-lattice Boltzmann studies for dendritic growth with natural convection," *Journal of Crystal Growth*, vol. 474, pp. 146–153, 2017.

[45] X. B. Qi, Y. Chen, X. H. Kang, D. Z. Li, and T. Z. Gong, "Modeling of coupled motion and growth interaction of equiaxed dendritic crystals in a binary alloy during solidification," *Scientific Reports*, vol. 7, p. 45770, 2017.

[46] D. Liu and Y. Wang, "Mesoscale multi-physics simulation of solidification in selective laser melting process using a phase field and thermal lattice boltzmann model," in *ASME 2017 International Design Engineering Technical Conferences and Computers and Information in Engineering Conference*, pp. V001T02A027–V001T02A027, American Society of Mechanical Engineers, 2017.

[47] A. K. Boukellal, J.-M. Debierre, G. Reinhart, and H. Nguyen-Thi, "Scaling laws governing the growth and interaction of equiaxed al-cu dendrites: A study combining experiments with phase-field simulations," *Materialia*, 2018.

[48] K. Fezi and M. Krane, "Uncertainty quantification in solidification modelling," in *IOP Conference Series: Materials Science and Engineering*, vol. 84, p. 012001, IOP Publishing, 2015.

[49] K. Fezi and M. Krane, "Uncertainty quantification of modelling of equiaxed solidification," in *IOP Conference Series: Materials Science and Engineering*, vol. 143, p. 012028, IOP Publishing, 2016.

[50] K. Fezi and M. J. M. Krane, "Uncertainty quantification in modelling equiaxed alloy solidification," *International Journal of Cast Metals Research*, vol. 30, no. 1, pp. 34–49, 2017.

[51] K. Fezi and M. J. M. Krane, "Uncertainty quantification in modeling metal alloy solidification," *Journal of Heat Transfer*, vol. 139, no. 8, p. 082301, 2017.

[52] A. Plotkowski and M. Krane, "Quantification of epistemic uncertainty in grain attachment models for equiaxed solidification," *Metallurgical and Materials Transactions B*, vol. 48, no. 3, pp. 1636–1651, 2017.

[53] V. Barthelmann, E. Novak, and K. Ritter, "High dimensional polynomial interpolation on sparse grids," *Advances in Computational Mathematics*, vol. 12, no. 4, pp. 273–288, 2000.

[54] E. Novak and K. Ritter, "Simple cubature formulas with high polynomial exactness," *Constructive approximation*, vol. 15, no. 4, pp. 499–522, 1999.

[55] H.-J. Bungartz and M. Griebel, "Sparse grids," *Acta numerica*, vol. 13, pp. 147–269, 2004.

[56] F. Nobile, R. Tempone, and C. G. Webster, "A sparse grid stochastic collocation method for partial differential equations with random input data," *SIAM Journal on Numerical Analysis*, vol. 46, no. 5, pp. 2309–2345, 2008.

[57] S. A. Smolyak, "Quadrature and interpolation formulas for tensor products of certain classes of functions," in *Doklady Akademii Nauk*, vol. 148, pp. 1042–1045, Russian Academy of Sciences, 1963.

[58] G. W. Wasilkowski and H. Woźniakowski, "Explicit cost bounds of algorithms for multivariate tensor product problems," *Journal of Complexity*, vol. 11, no. 1, pp. 1–56, 1995.

[59] C. W. Clenshaw and A. R. Curtis, "A method for numerical integration on an automatic computer," *Numerische Mathematik*, vol. 2, no. 1, pp. 197–205, 1960.

[60] D. Xiu and G. E. Karniadakis, "The Wiener–Askey polynomial chaos for stochastic differential equations," *SIAM Journal on Scientific Computing*, vol. 24, no. 2, pp. 619–644, 2002.

[61] H. N. Najm, "Uncertainty quantification and polynomial chaos techniques in computational fluid dynamics," *Annual Review of Fluid Mechanics*, vol. 41, pp. 35–52, 2009.

[62] R. Ghanem *et al.*, "Modal properties of a space-frame with localized system uncertainties," in *in 8th ASCE Specialty Conference of Probabilistic Mechanics and Structural Reliability, ASCE*, Citeseer, 2000.

[63] O. P. Le Maître, M. T. Reagan, H. N. Najm, R. G. Ghanem, and O. M. Knio, "A stochastic projection method for fluid flow: II. Random process," *Journal of computational Physics*, vol. 181, no. 1, pp. 9–44, 2002.

[64] M. T. Reagana, H. N. Najm, R. G. Ghanem, and O. M. Knio, "Uncertainty quantification in reacting-flow simulations through non-intrusive spectral projection," *Combustion and Flame*, vol. 132, no. 3, pp. 545–555, 2003.

[65] I. Steinbach, "Effect of interface anisotropy on spacing selection in constrained dendrite growth," *Acta Materialia*, vol. 56, no. 18, pp. 4965–4971, 2008.

[66] I. Steinbach, "Phase-field models in materials science," *Modelling and simulation in materials science and engineering*, vol. 17, no. 7, p. 073001, 2009.

[67] O. Shchyglo, E. Borukhovich, P. Engels, M. Stratmann, J. Görler, R. Schiedung, A. Monas, M. Tegeler, R. D. Kamachali, M. K. Rajendran, M. Boeff, D. Medvedev, S. Gladkov, R. Spatschek, and I. Steinbach, "Openphase." http://www.openphase.de.

[68] D. Medvedev, F. Varnik, and I. Steinbach, "Simulating mobile dendrites in a flow," *Procedia Computer Science*, vol. 18, pp. 2512–2520, 2013.

[69] M. Stoyanov, "User manual: TASMANIAN sparse grids," Tech. Rep. ORNL/TM-2015/596, Oak Ridge National Laboratory, One Bethel Valley Road, Oak Ridge, TN, 2015.

[70] M. K. Stoyanov and C. G. Webster, "A dynamically adaptive sparse grids method for quasi-optimal interpolation of multidimensional functions," *Computers & Mathematics with Applications*, vol. 71, no. 11, pp. 2449–2465, 2016.

[71] M. Stoyanov, "Hierarchy-direction selective approach for locally adaptive sparse grids," Tech. Rep. ORNL/TM-2013/384, Oak Ridge National Laboratory, One Bethel Valley Road, Oak Ridge, TN, 2013.

[72] M. Stoyanov, D. Lebrun-Grandie, J. Burkardt, and D. Munster, "Tasmanian," 9 2013.

[73] D. Tourret and A. Karma, "Growth competition of columnar dendritic grains: A phase-field study," *Acta Materialia*, vol. 82, pp. 64–83, 2015.

[74] R. Bostanabad, Y. Zhang, X. Li, T. Kearney, L. C. Brinson, D. W. Apley, W. K. Liu, and W. Chen, "Computational microstructure characterization and reconstruction: Review of the state-of-the-art techniques," *Progress in Materials Science*, 2018.

[75] Y. Liu, M. S. Greene, W. Chen, D. A. Dikin, and W. K. Liu, "Computational microstructure characterization and reconstruction for stochastic multiscale material design," *Computer-Aided Design*, vol. 45, no. 1, pp. 65–76, 2013.

[76] D. Li, "Review of structure representation and reconstruction on mesoscale and microscale," *JOM*, vol. 66, no. 3, pp. 444–454, 2014.

[77] S. Bargmann, B. Klusemann, J. Markmann, J. E. Schnabel, K. Schneider, C. Soyarslan, and J. Wilmers, "Generation of 3D representative volume elements for heterogeneous materials: A review," *Progress in Materials Science*, vol. 96, pp. 322–384, 2018.

[78] S. Suzuki *et al.*, "Topological structural analysis of digitized binary images by border following," *Computer vision, graphics, and image processing*, vol. 30, no. 1, pp. 32–46, 1985.

[79] G. Bradski, "The OpenCV Library," *Dr. Dobb's Journal of Software Tools*, 2000.

[80] A. S. Barros, I. A. Magno, F. A. Souza, C. A. Mota, A. L. Moreira, M. A. Silva, and O. L. Rocha, "Measurements of microhardness during transient horizontal directional solidification of Al-rich Al-Cu alloys: Effect of thermal parameters, primary dendrite arm spacing and Al_2Cu intermetallic phase," *Metals and Materials International*, vol. 21, no. 3, pp. 429–439, 2015.

[81] B. J. Debusschere, H. N. Najm, P. P. Pébay, O. M. Knio, R. G. Ghanem, and O. P. Le Maître, "Numerical challenges in the use of polynomial chaos representations for stochastic processes," *SIAM Journal on Scientific Computing*, vol. 26, no. 2, pp. 698–719, 2004.

[82] B. Debusschere, K. Sargsyan, C. Safta, and K. Chowdhary, "Uncertainty quantification toolkit (UQTk)," *Handbook of Uncertainty Quantification*, pp. 1–21, 2016.